Studies of Lorentz Violation using Air Shower Data

Masterarbeit
zur Erlangung des akademischen Grades
Master of Science
(M.Sc.)

der Universität Siegen

Department Physik

vorgelegt von
Fabian Dünkel

Juli 2019

Contents

1. Introduction

The Standard Model of Particle Physics (SM) and its predictions have been tested to very high precision. However, it is known that the SM is incomplete, since it does not, for example, describe gravity or dark matter. Current approaches to establish a more comprehensive and fundamental theory allow for deviations from exact Lorentz symmetry. Under exact Lorentz symmetry the laws of physics are invariant under Lorentz transformation and thus independent of the inertial frame of the observer. Current bounds for Lorentz Violation (LV) in various sectors of the SM often take advantage of the high energies of cosmic rays and gamma rays (see e.g. [1, 2]).

In this thesis, the impact of LV on extensive air showers which are initiated by cosmic rays in the Earth's atmosphere is studied, with a focus on ultra-high energies. Here, isotropic nonbirefringent LV in the photon sector is considered for the case of a photon velocity greater than the maximum attainable velocity of standard fermions.

The changes caused by this were first explored in [3], where the Heitler model for electromagnetic cascades was modified by including Lorentz-violating photon decays. A significant change in the longitudinal shower development was found.

Building upon these results, a full Monte Carlo (MC) procedure was used to study the impact of LV on electromagnetic cascades initiated by hadrons [1]. Under the conservative assumption of a pure proton composition of cosmic rays, a limit on LV was determined comparing the average atmospheric depth of the shower maximum of the modified MC simulations to measured values by the Pierre Auger Observatory [4]. For these simulations, the MC code CONEX v2r5p40 [5, 6] was modified to accomodate the differences between the SM and the model allowing LV.

In this thesis, the full MC approach is expanded, taking into account the composition of cosmic rays, which do not solely consist of protons. To achieve this, air shower simulations for different elements are produced and the results are combined using varying weights for each element. In addition, shower fluctuations are used as an additional parameter to determine reasonable partitions of each element. Using these expansions upon the previous method, a stricter limit on LV can be determined.

2. Modified Maxwell Theory

The model used in this thesis is a relatively simple extension of standard Quantum Electrodynamics (QED). The Lagrange density is modified by adding a single term which breaks Lorentz invariance but preserves CPT and gauge invariance [7, 8]:

$$\begin{aligned}\mathcal{L} = &-\frac{1}{4}F^{\mu\nu}(x)F_{\mu\nu}(x) \\ &+\bar{\Psi}(x)(\gamma^{\mu}[i\delta_{\mu} - eA_{\mu}(x)] - m)\Psi(x) \\ &-\frac{1}{4}(k_F)_{\mu\nu\rho\sigma}F^{\mu\nu}(x)F^{\rho\sigma}(x).\end{aligned} \tag{2.1}$$

The last term on the right-hand side gives the newly introduced CPT-invariant LV in the photon sector[1], while the first two terms correspond to standard QED. The Minkowski metric $\eta_{\mu\nu} = [\mathrm{diag}(1,-1,-1,-1)]_{\mu\nu}$ and its inverse $\eta^{\mu\nu}$ are used to lower or raise indices throughout the entire thesis. Furthermore, natural units ($\hbar = c = 1$) are used to simplify formulaic expressions. The Maxwell field tensor is defined as usual as $F_{\mu\nu} = \delta_{\mu}A_{\nu} - \delta_{\nu}A_{\mu}$.

The newly added constant tensor $(k_F)_{\mu\nu\rho\sigma}$ in (2.1) has twenty independent components. Of those, ten produce birefringence and eight lead to direction-dependent modifications of the photon propagation. The two remaining components correspond to an isotropic modification of photon propagation and an unobservable double trace which leads to changes in the normalisation of the photon field. Isotropic non-birefringent LV in the photon sector is then controlled by a single, dimensionless parameter κ, which relates to the tensor $(k_F)_{\mu\nu\rho\sigma}$ in the following way:

$$(k_F)_{\mu\nu\rho\sigma} = \frac{1}{2}(\eta_{\mu\rho}\tilde{\kappa}_{\nu\sigma} - \eta_{\mu\sigma}\tilde{\kappa}_{\nu\rho} + \eta_{\nu\sigma}\tilde{\kappa}_{\mu\rho} - \eta_{\nu\rho}\tilde{\kappa}_{\mu\sigma}), \tag{2.2}$$

$$\tilde{\kappa}_{\mu\nu} = \frac{\kappa}{2}[\mathrm{diag}(3,1,1,1)]_{\mu\nu}. \tag{2.3}$$

Here, (2.2) gives nonbirefringence and (2.3) produces isotropy. The parameter κ can only take values in the halfopen interval (-1,1], a restriction set by microcausality and unitarity [9]. Note that the parameter κ is denoted by $\tilde{\kappa}_{\mathrm{tr}}$ in several references [9].

[1] The CPT transformation is the simultaneous operation of charge conjugation (C), parity reflection (P) and time reversal (T).

The field equations obtained from (2.1) and (2.2) determine the photon propagation, which results in a change of the phase velocity given by:

$$v_{\mathrm{ph}} = \frac{\omega}{|\vec{k}|} = \sqrt{\frac{1-\kappa}{1+\kappa}}c \tag{2.4}$$

The velocity c corresponds here to the highest possible attainable velocity of the massive Dirac fermion of (2.1). If the value of κ is positive (negative), then the photon velocity is smaller (larger) than c. κ can also be defined using the relative difference between the squared maximum fermion velocity and the squared photon velocity:

$$\kappa = \frac{c^2 - (v_{\mathrm{ph}})^2}{c^2 + (v_{\mathrm{ph}})^2} \sim 1 - \frac{v_{\mathrm{ph}}}{c}. \tag{2.5}$$

As mentioned above, natural units are used, setting $c = 1$.
If the photon velocity differs from the photon velocity of the standard model, which corresponds to a nonzero value of κ, certain classically forbidden decay processes become allowed. The theory behind these processes as well as detailed calculations of the later discussed processes can be found for example in [2, 10].

Here, the focus is on negative values of κ, which means having a photon velocity greater than the maximum attainable velocity of the standard Dirac fermion. In the case of negative κ, relevant changes in two decay processes appear: The first one is a change in the decay rate of photons above a certain energy threshold, the second is a change in the neutral pion decay.

With sufficiently high energy, the nonstandard photon, denoted by $\tilde{\gamma}$, can decay into an electro-positron pair:

$$\tilde{\gamma} \to e^- + e^+ \tag{2.6}$$

The specific energy threshold, as calculated in [2], for this photon decay is given by

$$E_\gamma^{\mathrm{thresh}}(\kappa) = 2m_e\sqrt{\frac{1-\kappa}{-2\kappa}} \sim \frac{2m_e}{\sqrt{-2\kappa}} \tag{2.7}$$

The energy threshold is given in terms of the electron rest mass $m_e \approx 0.511\,\mathrm{MeV}$ and is dependent on κ. The exact decay rate of the photon decay Γ_{PhD} has been calculated [2, 11] as a function of the photon energy $E_\gamma \geq E_\gamma^{\mathrm{thresh}}$

$$\Gamma_{\mathrm{PhD}}(E_\gamma) = \frac{\alpha}{3}\,\frac{-\kappa}{1-\kappa}\,\sqrt{(E_\gamma)^2 - (E_\gamma^{\mathrm{thresh}})^2} \times \left(2 + \left(\frac{E_\gamma^{\mathrm{thresh}}}{E_\gamma}\right)^2\right). \tag{2.8}$$

The value of E_γ^{thresh} is taken from (2.7) and $\alpha \approx 1/137$ is the fine-structure constant. The relation between decay rate and decay length of the photon is given by

$$l_{\mathrm{PhD}} = \frac{c}{\Gamma_{\mathrm{PhD}}}. \tag{2.9}$$

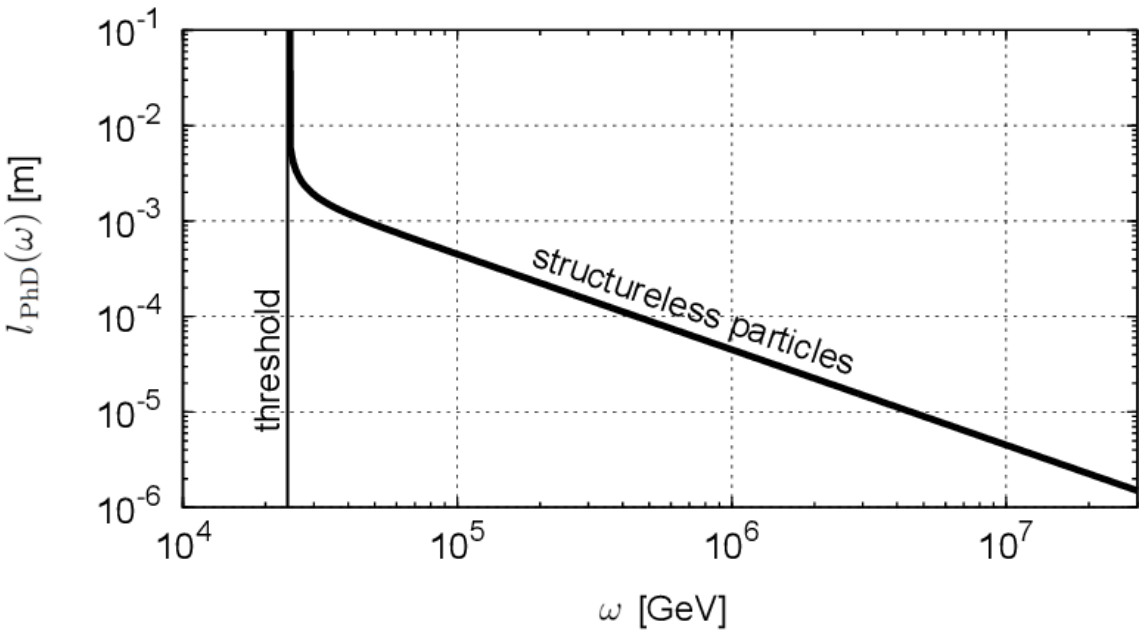

Figure 2.1.: *Photon decay length l_{PhD} given in meters for the $\tilde{\gamma} \to e^- + e^+$ process with $\kappa = -9 \times 10^{-16}$ [11].*

The decay length of the photon drops right above the energy threshold to scales of centimeters (see Fig. 2.1) which can be treated as a quasi-instantaneous conversion of the photon into a electron-positron pair. This new property of the photon decay can be used to impose bounds on negative κ, for example by using ground-based Cherenkov-telescope observations of gamma rays with energies of order 10 to 100 TeV.

Since the air showers studied in later chapters are induced by hadrons, possible modifications of other processes due to LV have to be taken into account. The relevant process in this case is the decay of the neutral pion into two non-standard photons:

$$\pi^0 \to \tilde{\gamma} + \tilde{\gamma}. \tag{2.10}$$

In the context of the modified Maxwell theory used here, the decay time of the neutral pion is modified as follows [10]:

$$\tau(E_{\pi^0}, \kappa) = \frac{\tau_{\mathrm{SM}}}{g(E_{\pi^0}, \kappa)}. \tag{2.11}$$

The modification is done by introducing the factor $g(E_{\pi^0}, \kappa)$, which is depending on the energy E_{π^0} of the neutral pion and the LV parameter κ, by which the decay time τ_{SM} in the conventional Lorentz invariant theory is modified. This factor is given by

$$g(E_{\pi^0}, \kappa) = \begin{cases} \frac{\sqrt{1-\kappa^2}}{(1-\kappa)^3}[1 - \frac{(E_{\pi^0})^2 - (m_{\pi^0})^2}{(E_{\pi^0}^{cut})^2 - (m_{\pi^0})^2}]^2 & \text{for } E_{\pi^0} < E_{\pi^0}^{cut}, \\ 0 & \text{otherwise.} \end{cases} \tag{2.12}$$

The pion cutoff energy $E_{\pi^0}^{\text{cut}}$ used in (2.12) is given by

$$E_{\pi^0}^{\text{cut}} = m_{\pi^0}\sqrt{\frac{1-\kappa}{-2\kappa}} \sim m_{\pi^0}\frac{1}{\sqrt{-2\kappa}} \sim \frac{m_{\pi^0}}{2m_e}E_\gamma^{\text{thresh}} \approx 132 E_\gamma^{\text{thresh}}. \tag{2.13}$$

The asymptotic photon threshold from (2.7) was used and the numerical values for both electron ($m_e \approx 0.511\,\text{MeV}$) and neutral pion ($m_{\pi^0} \approx 135\,\text{MeV}$) rest masses were set in. The result from (2.13) implies that the effects of LV on neutral pions can be seen at energies which are more than two orders of magnitude above the photon decay threshold E_γ^{thresh}.

2.1. Previous Bounds on Lorentz Violation

The most stringent Earth-based bound up to now on isotropic non-birefringent LV using observations of gamma rays is given in [2] as:

$$\kappa > -9 \times 10^{-16} (98\,\%\ \text{C.L.}) \tag{2.14}$$

This limit was reached through the analysis of the highest energies of the detected gamma-ray photons. Since the photons that were measured existed it follows that they did not decay before that time. For photons above E_γ^{thresh}, this would mean that they travelled parsecs with a decay length of only centimeters. This sets a lower limit on the possible values of the minimum energy for nonstandard photon decay $E_\gamma^{\text{thresh}} \geq E_\gamma^{\text{measured}}$, which implies a bound on the possible values of κ. In order to improve this bound using the same method, photons of higher energies have to be detected. However the prospects of measuring such photons are unclear [12].

This bound was improved in [1] by expanding the analysis to include secondary photons in air showers initiated by primary hadrons. The new bound was reached using LV-modified code of the air shower simulation CONEX to compare results with LV to actual measurements of the Pierre Auger Observatory [4]. This produced a new lower bound on κ which is more than two orders of magnitude closer to zero than the one given in (2.14):

$$\kappa > -3 \times 10^{-19} (98\,\%\ \text{C.L.}) \tag{2.15}$$

3. Cosmic Rays

The Earth is hit by billions of particles of extraterrestrial origin each second, ranging everywhere from light neutrinos originating from our sun to heavy iron nuclei from Active Galactic Nuclei (AGN) lightyears away. The term cosmic rays refers only to charged particles of cosmic origin due to historic reasons. These include stable nuclei such as protons or iron as well as light elementary charged particles like positrons and electrons. Two main properties of cosmic rays are the elemental composition and the energy spectrum of all cosmic rays arriving at the Earth. Those two properties will be covered in the next two sections. When primary cosmic rays arrive at the Earth they interact with the atmosphere, producing cascades of secondary particles. These extensive air showers are described in Sec. 3.3.

3.1. Elemental Composition

Determining the elemental composition of primary cosmic rays is not an easy task. Up to energies around 100 TeV, direct measurements of cosmic rays are possible e. g. using high-altitude balloons or satellite experiments. At higher energies direct measurements of cosmic rays before any interactions with Earth's atmosphere are not feasible due to the highly reduced flux (see Sec. 3.2). This leaves only indirect measurements of extensive air showers for cosmic rays of the highest energies. Due to the indirect measurement the properties of the primary particle need to be reconstructed from the recorded shower data, whose interpretation is highly dependent on the interaction model used. But all current models become less precise at higher energies. In spite of these problems, the study of the composition of cosmic rays can be very useful to help revealing their origins and acceleration mechanisms.

The largest portion of cosmic rays are protons and nuclei which make up around 98 % of all cosmic rays while the remaining 2 % are electrons. The protons and nuclei are mainly protons (87 %), around 12 % are helium nuclei, while all heavier nuclei combine to the remaining 1 %. The composition of hadronic cosmic rays in relation to their relative abundance is shown in Fig. 3.1.

Hydrogen and Helium are much more frequently found in the solar system than in Galactic Cosmic Rays (GCRs). Since the ionisation energies of these elements are fairly

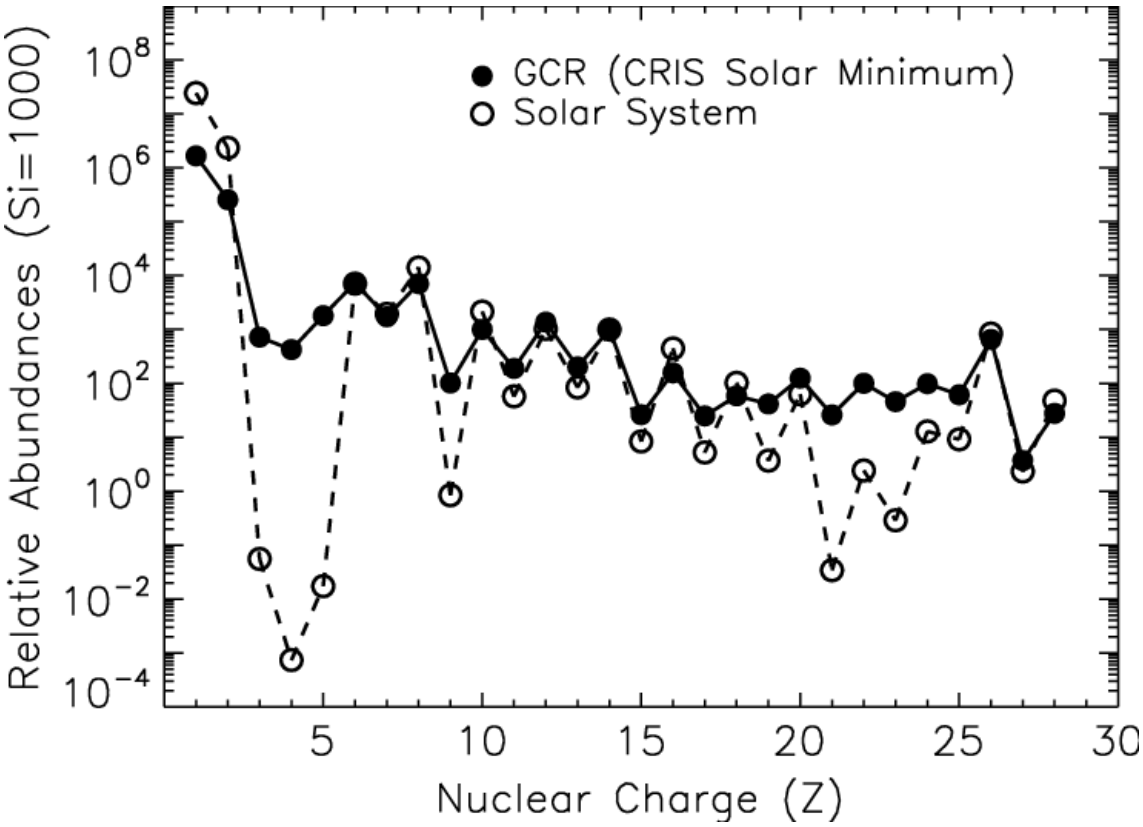

Figure 3.1.: *Relative abundance of different elements in galactic cosmic rays (filled circles) and the solar system (empty circles). All values were normalized to the relative abundance of Si($Z = 14$) at 10^3. [13]*

high, it is a reasonable assumption that some of the formed particles are unionized. However, most acceleration mechanisms affect charged particles only, thus a considerable fraction of helium and hydrogen particles would not be accelerated and only ionized particles would reach us.

Two groups of heavier elements (Li, Be, B and Sc, Ti, V) are more common in GCRs than in hadrons from the solar system. This can be explained by them being spallation products of the collision of GCRs with interstellar matter which are then further accelerated, thus explaining the relative abundance in GCRs.

These elemental compositions have been mostly determined using direct observations of low energy cosmic rays, which make up the majority of cosmic rays arriving at the Earth. However, at higher energies the exact composition of cosmic rays is still unknown and remains subject of research.

3.2. Energy Spectrum

Cosmic rays have a very wide energy spectrum extending over more than ten orders of magnitude in energy. The flux of cosmic rays decreases by about three orders for each order of magnitude gained in energy, resulting in a flux range spanning thirty orders of magnitude. The differential flux of cosmic rays depending on energy can be approximated by a broken power law:

$$\frac{\mathrm{d}\Phi}{\mathrm{d}E} \propto E^{-\gamma} \tag{3.1}$$

The spectral index γ is approximately constant for wide ranges of the energy spectrum [14], as can be seen in Fig. 3.2. At energies below 3 PeV the spectral index is $\gamma \approx -2.7$. At this energy the knee is reached, after which the spectral index increases to $\gamma \approx -3.1$. A less pronounced second knee can be seen in some measurements where a further steepening of the spectrum happens, followed by the ankle at 4×10^{18} eV where the spectrum flattens back again to $\gamma \approx -2.7$.

The exact origins of the ankle as well as the knee are not yet fully understood and are still subject of research. Results of air-shower experiments suggest the knee exists due to a reduced abundance of light elements in cosmic rays [16], another possibility is that the knee is erroneously induced due to unknown mechanisms in the shower detection process [17]. One interpretation of the ankle is as a transition from sources inside our galaxy to extragalactic sources with a different composition [18].

3.3. Extensive Air Showers

Entering the Earth's atmosphere, cosmic rays can interact with atmospheric particles, in most cases nitrogen nuclei. In this first interaction, many secondary particles are produced, which themselves can again interact with the atmosphere. In each generation of this extensive air shower, the secondary particles carry less energy per particle. The total number of particles inside the shower increases until the shower maximum is reached at an atmospheric depth of X_{max}, where the energy of most secondary particles is too small to produce new particles. Below this point, the number of secondary particles decreases. X_{max} is an important property of the air shower which depends on the type of primary particle entering the atmosphere and its energy. The first interactions in the atmosphere are crucial for the further development of the shower. A simple depiction of the main processes taking place during shower development can be seen in Fig. 3.3.

The particles produced by the shower during the propagation through the atmosphere form a curved disc propagating just below the speed of light. The thickness of the disk is

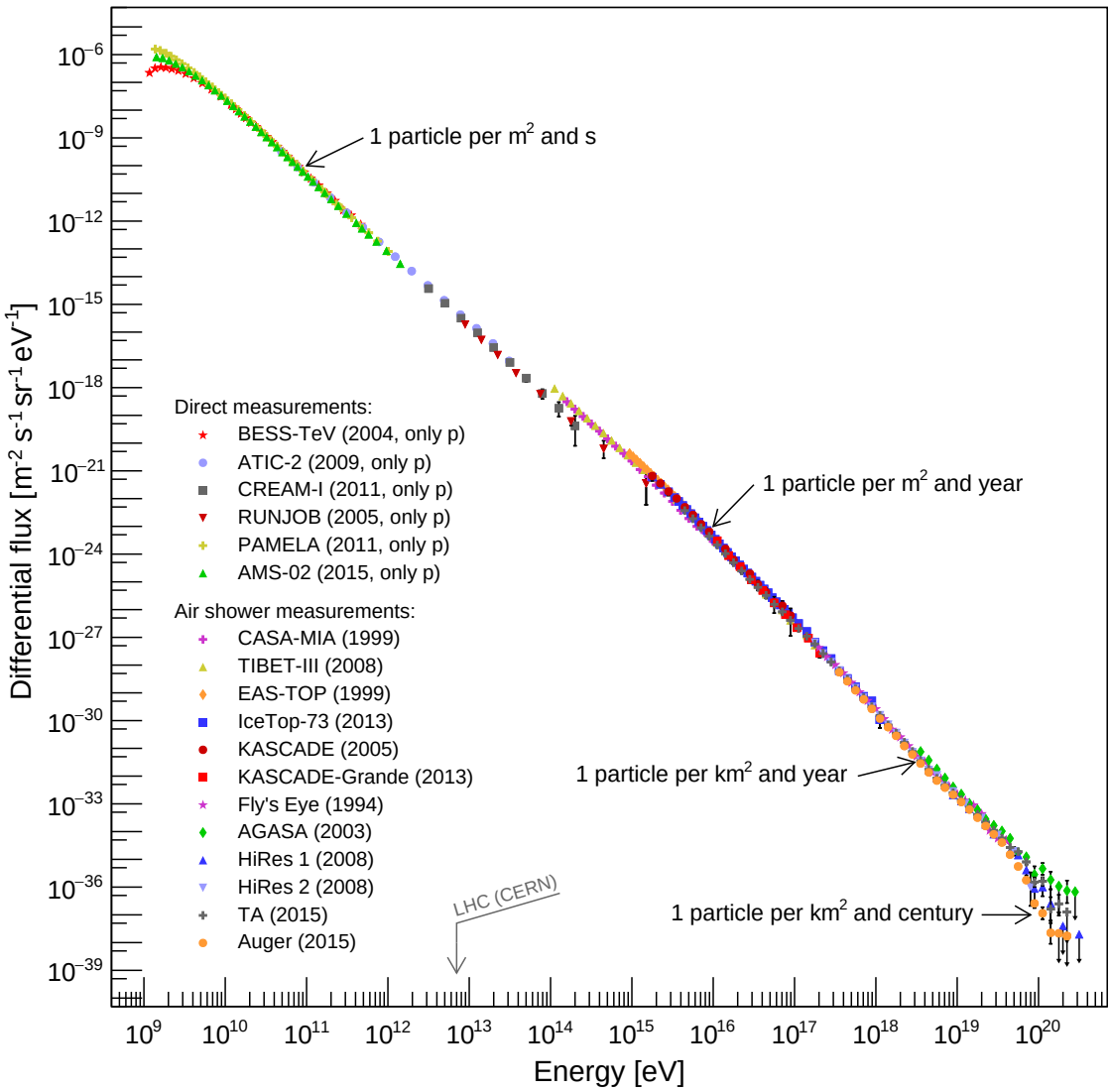

Figure 3.2.: *The measured all-particle energy spectrum of primary cosmic rays [15]. The spectrum was measured with detectors above the atmosphere (for low energies) as well as with earth-bound air-shower detectors.*

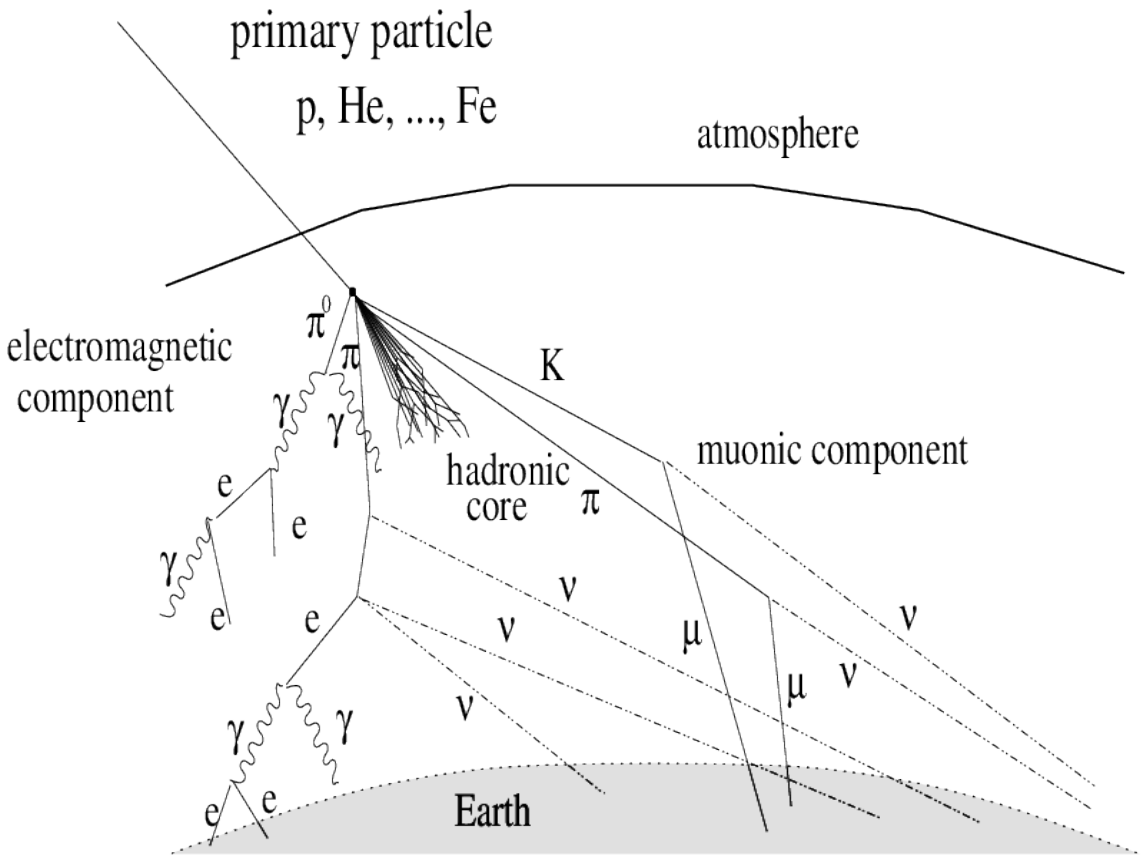

Figure 3.3.: *Schematic view of the processes within an air shower initiated by a primary hadron [19]. The hadronic core as well as the electromagnetic and muonic components are displayed seperately.*

in the order of magnitude of meters, while the surface of the disc spans square kilometers. Most of the particles are situated near the center of the disk, which is also the shower axis, while the disk thickens towards the edges. The total number of secondary particles contained in a typical proton-induced shower with a primary energy of 10^{15} eV is around one million (see e. g. [20]). Most of these particles can be classified into one of three categories: the hadronic, electromagnetic or muonic components.

Only 1 % of particles in an extensive air shower are hadrons [21]. Because the first interaction between the cosmic-ray nucleus and the atmosphere, as well as the following cascade are hadronic, this small number of hadronic particles plays an important role in the shower development. This first interaction initiates a hadronic cascade of secondary particles, consisting mostly of pions, with less likely kaon production. Charged pions interact again with the atmosphere to produce more secondary particles, while neutral pions decay into photons via

$$\pi_0 \rightarrow \gamma + \gamma, \tag{3.2}$$

because of their high interaction length relative to their decay length. Further hadronic particles are produced until the energy of a single particle is less than the threshold for pion production. From then on the particles lose energy via electromagnetic interactions with the atmosphere until they decay and the hadronic cascade dies out. The transverse momenta of the particles of the hadronic cascade are very small compared to their total momentum, so they form a narrow cone around the trajectory of the primary particle with a diameter in the order of 10 m.

The photons, electrons and positrons of the air shower form the electromagnetic component. The first photons of the electromagnetic component are mostly produced by the decay of a neutral pion. These photons can interact with atmospheric nuclei and produce electron-positron pairs via

$$\gamma + \text{nucleus} \rightarrow e^+ + e^- + \text{nucleus}. \tag{3.3}$$

The electrons and positrons produced in this way can emit photons via bremsstrahlung:

$$e^\pm + \text{nucleus} \rightarrow e^\pm + \gamma + \text{nucleus}. \tag{3.4}$$

These processes take place as long as the interacting particle is above the threshold energy of the relevant process, thus forming an electromagnetic cascade. Other electromagnetic processes like the photoelectric or Compton effect can be neglected because of the very high energies of the particles in the cascade. Since there is not only one single photon starting the cascade, but many photons originating from neutral pion decays, the electromagnetic component of the shower is a superposition of all the electromagnetic cascades started by different particles. The electromagnetic component represents 89 % of the total number of particles in an extensive air shower. The short radiation lengths of electrons and photons lead to a rapid absorption of these particles and to a much higher lateral spread in comparison to the hadronic component. In the case of a non hadronic primary particle, a primary electron or photon can also initiate an electromagnetic cascade, without the prior forming of a hadronic component, making the air shower purely electromagnetic.

The third major component of an extensive air shower is the muonic component. Muons are produced in the decay of charged mesons of the hadronic component, e. g. via pion and kaon decay:

$$\begin{aligned} \pi^\pm &\rightarrow \mu^\pm + \nu_\mu(\bar{\nu}_\mu) \\ K^\pm &\rightarrow \mu^\pm + \nu_\mu(\bar{\nu}_\mu) \\ K^\pm &\rightarrow \pi^0 + \mu^\pm + \nu_\mu(\bar{\nu}_\mu). \end{aligned} \tag{3.5}$$

Most of the muons are produced in the early stages of the shower. This is due to the lower air density and longer interaction lengths in the upper atmosphere, resulting in a higher probability of a decay of the hadrons into muons. Muons are unaffected by the strong interaction and lose their energy mostly in electromagnetic interaction processes, enabling them to pass through the atmosphere almost undisturbed. The decay time of muons at high energies is affected by relativistic time dilation, such that high energy muons are able to reach the ground, however at low energies decay via

$$\mu^{\pm} \rightarrow e^{\pm} + \nu_e(\bar{\nu}_e) + \bar{\nu}_\mu(\nu_\mu) \tag{3.6}$$

before reaching the ground is probable, thus feeding the electromagnetic component. The propagation direction of the muons is mostly determined by the direction of the decaying charged mesons, since muons are mainly emitted along their line of flight and contributions of scattering are supressed by a factor of $(m_e/m_\mu)^2$ in comparison to electrons.

Muons account for about 10 % of the total number of particles in an extensive air shower, but due to the fact that they are able to pass the atmosphere nearly undisturbed, they comprise 80 % of all secondary particles measured at sea level. Due to muon decay and production neutrinos are produced in the muonic component, which are also able to pass the atmosphere undisturbed, but their interaction cross section is so small that they play only an inferior role in air shower measurements.

4. Pierre Auger Observatory

One of the major obstacles in the detection of cosmic rays is the rapid decrease of the flux at high energies. The flux of about one particle per square meter per second in the TeV regime drops to one particle per square kilometer per year in the EeV range and even less for higher energies. Therefore, only indirect measurements with air shower experiments are an option for the study of Ultra-High-Energy Cosmic Rays (UHECRs). Because of the very low flux at the highest energies very large areas have to be covered by the experiment to acquire the necessary amount of data in a reasonable time frame.

The Pierre Auger Observatory is an international air shower experiment which is specifically designed to study UHECRs at the EeV range. Several fundamental questions in astrophysics can be tackled by research at these energies, such as the energy spectrum and origin of UHECRs and their acceleration mechanisms. Since the direction of incoming particles is also measured, the Pierre Auger Observatory can also be used to determine anisotropies in the arrival directions of primary cosmic rays, which helps to reveal possible sources of cosmic rays.

To perform these measurements, the Pierre Auger Observatory consists of two independent detector systems: a Surface Detector (SD) array containing 1660 water Cherenkov tanks located at a distance of 1.5 km to each other, overlooked by four Fluorescence Detector (FD) telescope sites. The layout of the site can be seen in Fig. 4.1. The SD records the particles from an extensive air shower at the ground level, the fluorescence telescopes observe the ultraviolet fluorescence light which is produced by the interaction of the same air showers with the atmosphere. By combining both complementary techniques unprecedented accuracy is reached because of the possibility of cross-calibration between both detector components. Both the SD and the FD will be described in the following sections.

4.1. Surface Detector Array

The SD of the Pierre Auger Observatory was completed in 2008. The 1660 SD stations are positioned on a hexagonal grid at a distance of 1.5 km to each other, covering a total area of about 3000 km^2. Each detector station consists of a cylindrical polyethylene tank with a diameter of 3.6 m, filled with 11 m^3 of purified water as well as three Photo Multiplier Tubes

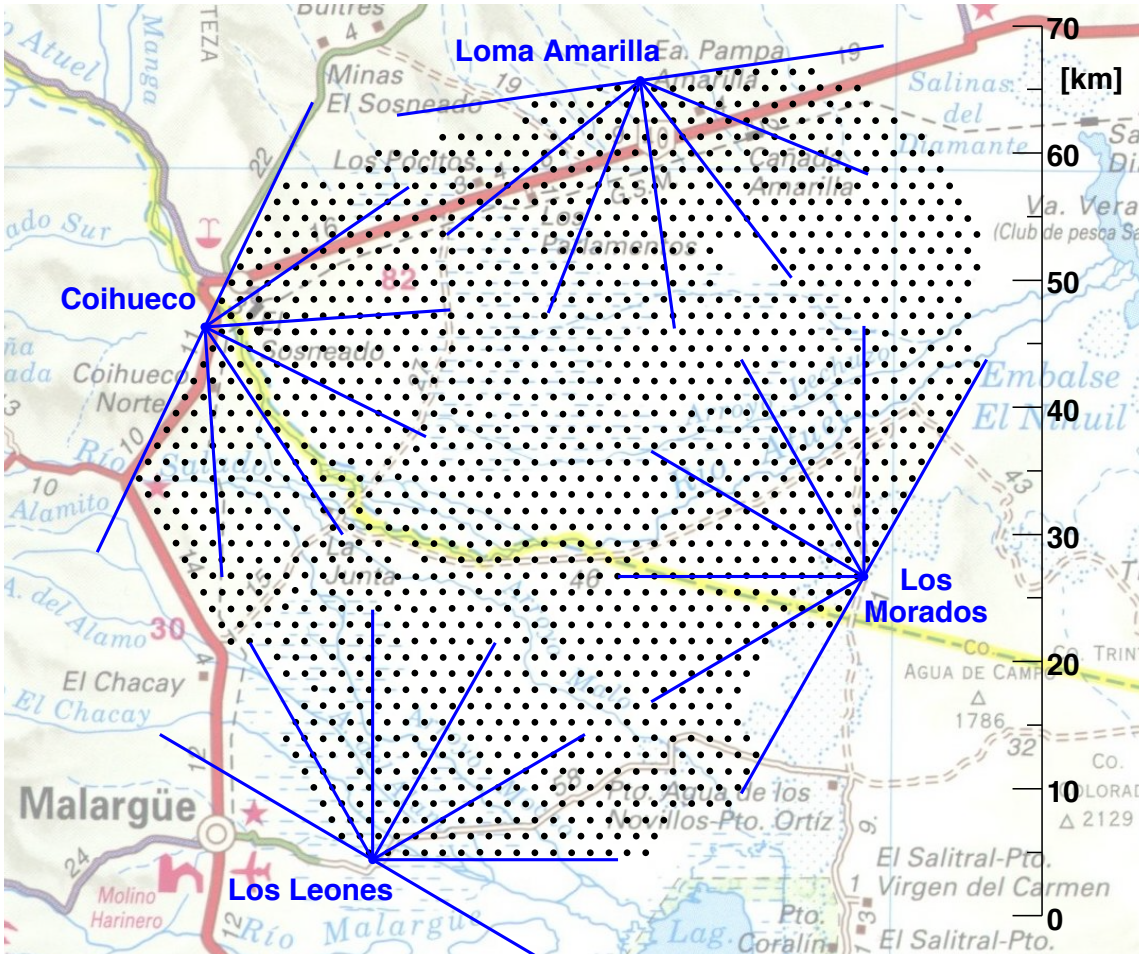

Figure 4.1.: *Schematic layout of the Pierre Auger Observatory site at Malargue, Argentina [22]. Each black dot represents the position of one SD site while the blue lines represent the fields of view of the 24 fluorescence telescopes at the four FD sites.*

(PMTs), which are optically coupled to the water. The three PMTs are symmetrically positioned at the top of the tank with a distance of 1.2 m to each other. Every detector station is designed to work autonomously, so each detector is equipped with a solar power system which provides the 10 W of average power required to run the readout electronics as well as a battery [23]. Communication with the Central Data Acquisition System (CDAS) is achieved wirelessly through one of the four communication beacons which are located near the FD sites at the perimeter of the SD. To synchronize the time between the detector stations and the CDAS and to provide precise information of the stations position, a Global Positioning System (GPS) device is installed at each of the stations. Due to their duty cycle of nearly 100 %, the SD provides most of the data recorded by the Pierre Auger Observatory. One SD station can be seen in front of a FD site in Fig. 4.2.

Charged particles passing through the tanks are detected through the Cherenkov effect [25]. Cherenkov light is emitted along the trajectory of a charged particle in a medium

Figure 4.2.: *Photograph of a water Cherenkov detector station from the SD of the Pierre Auger Observatory in front of one of the four FD sites [24].*

moving faster than the speed of light in that medium. The Cherenkov light produced in the tanks by secondary particles from air showers passing through the water, most of them muons or electrons, is detected by the three PMTs mounted at the top of the tanks and converted into current pulses. A reflective layer of polyethylene fabric covers the inside of the tanks to increase the signal intensity. The PMT signals are read out and digitized by Flash Analog-to-Digital Converters (FADCs) at a rate of 40 MHz and stored for 100 s to be sent to the CDAS if requested [23].

A hierarchical trigger system is used to manage the large amounts of data inherent to such a large experiment [26]. The first two trigger levels (T1 and T2) are formed at the detector stations themselves. Those are then combined at the CDAS to check for correlations between them. This T3 trigger sent by the CDAS initiates data acquisition. The collected data is then further refined offline by using e. g. the incident times at different detector stations to determine the propagation direction of the air shower.

Since all detector stations have to work independently, they are designed to calibrate themselves using muon signals. This calibration is performed by comparing a measured spectrum to the known energy distribution of muons. The signal strength is measured in units of Vertical Equivalent Muons (VEM), where 1 VEM corresponds to the signal strength of a single muon traversing the tank vertically. Using this unit as a reference, the PMTs can be adjusted by regulating their high voltages to produce matching signals at all detector stations.

4.2. Fluorescence Detector

The FD of the Pierre Auger Observatory records the longitudinal shower development in the atmosphere above the SD array to complement the SD measurements of the lateral shower profile on ground level and enable crosschecks between both detectors. The FD consists of four sites at the perimeter of the SD array, each with six fluorescence telescopes having a field of view of $30° \times 30°$. The observation direction of the respective center is inclined to 16°. This results in a total field of view of $180° \times 30°$ for each of the FD sites, aligned towards the inside of the SD array, observing the sky between 1° and 31° elevation [27].

The fluorescence telescopes are modified Schmidt cameras. The light emitted by the air shower enters the telescope through a UV-passing window and an aperture system and is then reflected by a segmented mirror onto a pixel camera consisting of 440 PMTs. This signal is read out electronically. Absolute calibrations of the fluorescence telescope using a light source of known intensity are done yearly while relative calibrations using light-emitting diodes are done once every night.

The UV light measured by the FD is produced through the excitation of nitrogen molecules in the atmosphere by secondary particles of extensive air showers. When the excited molecules fall back to their ground states, UV light is emitted. This light is detected by the fluorescence telescopes as a calorimetric measure of the longitudinal shower profile. From this the primary energy of the primary cosmic ray can be reconstructed. Therefore it is crucial to exactly record the fluorescence light from the shower. The duty cycle of the FD is about 13%, because it is limited to operation in clear, moonless, cloudless nights only. The intensity of the detected fluorescence light also depends on the atmospheric conditions over the site, such as temperature, pressure and humidity, which are constantly monitored.

The event reconstruction of the FD is performed off-line. All PMT pixels which are corresponding to the shower are identified first and used to reconstruct the plane spanned by the axis of the recorded shower and the position of the fluorescence telescope. This is combined with the arrival times of the shower front as measured by the SD as well as the arrival times and yield of the shower light at the individual PMTs to achieve a three-dimensional reconstruction of the shower geometry.

5. Air Shower Simulations with CONEX

To produce the air shower simulations used by the later analysis, a modified version of the simulation program CONEX [5] is used. The CONEX code is a hybrid simulation code which combines MC simulations of high energy interactions in the early stages of the air shower with a fast numerical solution of cascade equations for the distributions of secondary particles in the later stages. The result is a fast one-dimensional simulation of shower profiles, including the average atmospheric depth of the shower maximum $\langle X_{\max} \rangle$ and shower fluctuations $\sigma(X_{\max})$. The details of isotropic, nonbirefringent Lorentz violation have been worked out in Cha. 2. For $\kappa < 0$, the nonstandard photon becomes unstable above the threshold $E_\gamma^{\text{thresh}}(\kappa)$, decaying into an electron-positron pair. The decay time of the neutral pion π^0 is also affected by Lorentz violation.

The basis for implementation of LV into the CONEX code is the version 2r5.40, which includes the most up-to-date interaction models EPOS LHC [28], QGSJET-II-04 [29] and SIBYLL 2.3 [30], although only the model EPOS LHC is used in this analysis. The original CONEX code is only modified in the MC part, specifically in the EGS4 part, where the MC simulation of the electromagnetic shower part is handled. The modification in the photon sector is the addition of an instantaneous decay of the photon into a electron-positron pair, if the energy of the photon is above the threshold $E_\gamma^{\text{thresh}}(\kappa)$. The sum of the energies of the electron and positron has to be equal to the energy of the decaying photon, while the energy of the electron is drawn randomly from a predetermined energy spectrum, dependent on κ and the photon energy.

The difference in pion decay time is implemented by adding an additional factor. The decay time for the neutral pion determined by the unmodified CONEX code is multiplied by the factor determined in (2.11) and (2.12), which is depending on the pion energy and κ. The effects of those modifications on $\langle X_{\max} \rangle$ and $\sigma(X_{\max})$ of proton induced air showers using different values of κ are clearly shown in Figs. 5.1 and 5.2. Below the energy threshold for the near-instant photon decay, no changes in $\langle X_{\max} \rangle$ or $\sigma(X_{\max})$ are seen, as expected according to the theory. Once photons above the energy threshold appear in the simulated showers, the $\langle X_{\max} \rangle$-value is significantly lower than the SM-value, with a greater impact on $\langle X_{\max} \rangle$ for more negative values of κ. Neutral pions become stable at sufficiently high energies and this change is occuring at energies approximately two orders of magnitude above the photon decay energy threshold as expected due to (2.13). This has only a minor effect on $\langle X_{\max} \rangle$, which can be seen as a slight upturn of the modified curve

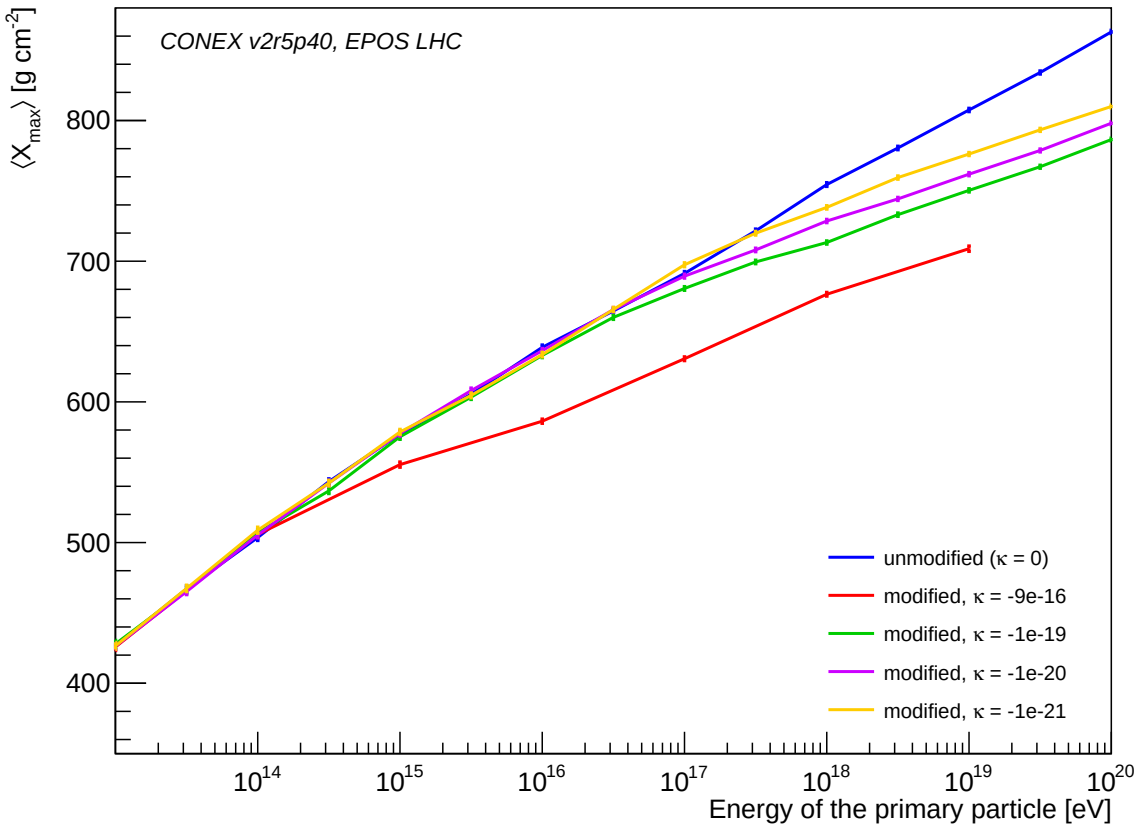

Figure 5.1.: *$\langle X_{max} \rangle$-values for protons over the entire analyzed energy spectrum, for different values of κ. It can be seen that the energies at which the modification due to LV are noticed increase for values of κ closer to 0. The value of $\kappa = -9 \times 10^{-16}$ is not relevant for the following analysis, but was only included to show the existing trends more clearly. For this reason there are also less data points at this κ value.*

two decades above the photon effects in Fig. 5.1. But for $\sigma(X_{\max})$ no changes between the different κ-values can be seen apart from statistical fluctuations in Fig. 5.2. This is understandable since the dominating influence on the fluctuations is the first interaction of the initial hadronic particle, which is not modified by LV. The same qualitative effects can be observed for the other simulated elements as well, while higher energies are needed to notice the effect of LV with heavier elements.

Since it is unreasonable to use mixtures of all possible combinations of all possible elements for the analysis, only four elements are used, representing the mass scale. In this case protons ($m = 1\,\mathrm{u}$) are used as a representative for the lightest elements, iron ($m = 56\,\mathrm{u}$) for the heaviest and in-between there are helium ($m = 4\,\mathrm{u}$) and oxygen ($m = 16\,\mathrm{u}$). Helium and oxygen were chosen because helium is a common primary particle for cosmic rays and the oxygen mass is logarithmically halfways between the helium and iron masses. The primary energies for which CONEX is used to produce datasets range from $10^{13}\,\mathrm{eV}$

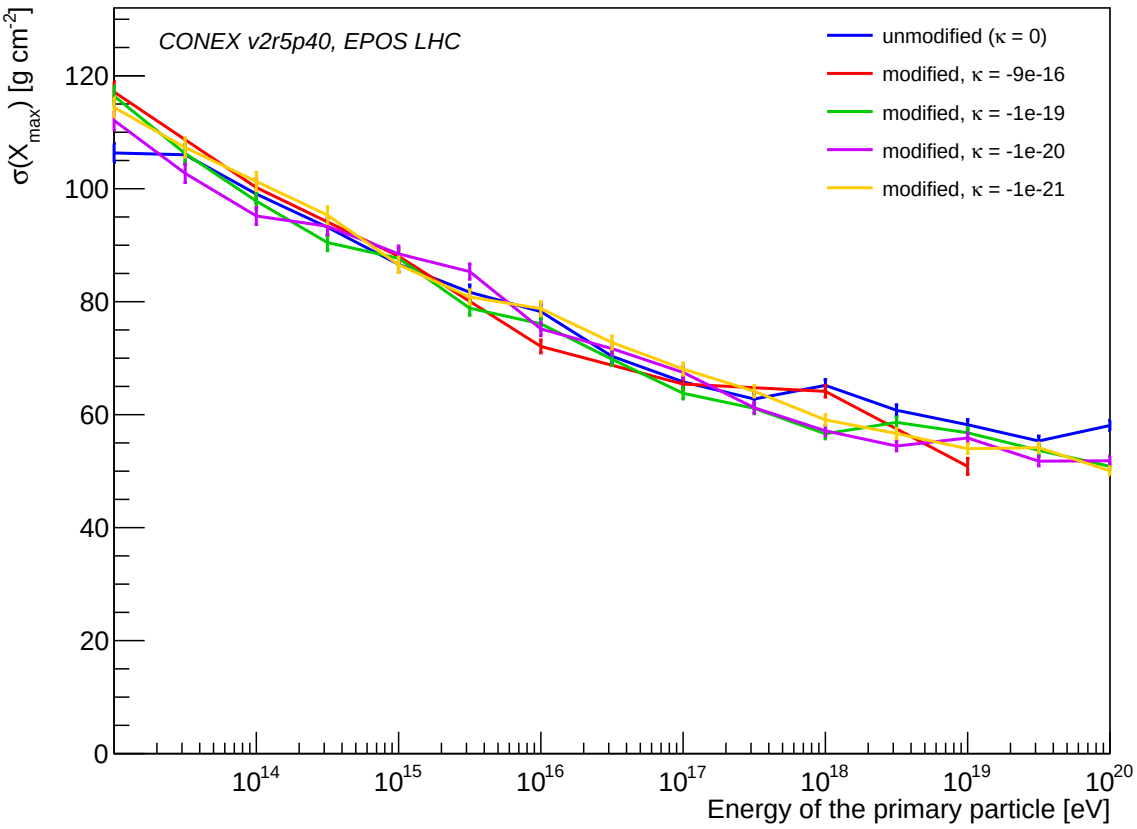

Figure 5.2.: *$\sigma(X_{max})$-values for protons over the entire analyzed energy spectrum, for different values of κ. Apart from the expected fluctuations due to statistic uncertainties the $\sigma(X_{max})$-values do not change significantly for different values of κ.*

to 10^{20} eV with stepsizes between energies of a factor of 0.5 in $log_{10}(E)$. For each of these energies, 2000 showers are simulated to be used in the later analysis.

A comparison to earlier simulations used in [1] was done to check the modified CONEX simulation code. One parameter used to compare both sets of simulations is the rescaled difference D between the values of $\langle X_{\max}\rangle$ for both cases, given by

$$D = \frac{|\langle X_{\max}\rangle_{\text{old}} - \langle X_{\max}\rangle_{\text{new}}|}{\sqrt{(\sigma(\langle X_{\max}\rangle_{\text{old}}))^2 + (\sigma(\langle X_{\max}\rangle_{\text{new}}))^2}}. \tag{5.1}$$

The values of this parameter for all energies at $\kappa = -1 \times 10^{21}$ can be seen in Fig. 5.3. Lower values of D correspond to a higher agreement between both simulations. In the case displayed in Fig. 5.3 more than half of the points are at $D < 1$, indicating a reasonable agreement between both sets of simulations.

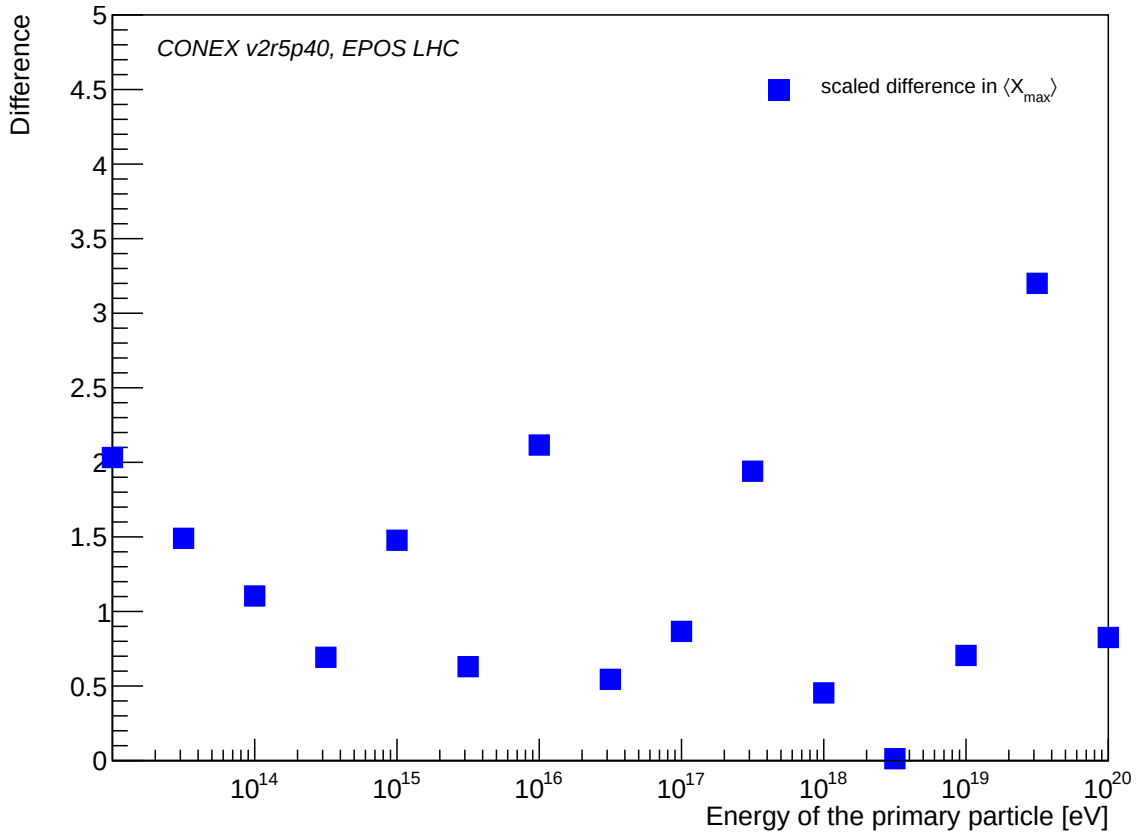

Figure 5.3.: *Visual presentation of* $D = \frac{|\langle X_{max}\rangle_{old} - \langle X_{max}\rangle_{new}|}{\sqrt{(\sigma(\langle X_{max}\rangle_{old}))^2 + (\sigma(\langle X_{max}\rangle_{new}))^2}}$. *The values of* $\langle X_{max}\rangle_{old}$ *are derived from the CONEX simulations used in [1], while* $\langle X_{max}\rangle_{new}$ *are the values of the modified CONEX simulations used here.*

The modifications in the neutral pion decay time are also noticed in the average number of ground muons in the modified simulations. Since neutral pions above the cutoff energy $E_{\pi^0}^{\text{cut}}$ can interact again, the average number of mouns increases at higher energies due to those interactions. The effect of the implemented LV on the muon number can be seen in Fig. 5.4. The energies at which the muon numbers are affected rise when κ is closer to 0, which is reasonable considering the dependence of $E_{\pi^0}^{\text{cut}}$ on κ ($E_{\pi^0}^{\text{cut}} \sim \frac{1}{\sqrt{\kappa}}$). The muon excess steadily grows with the energy.

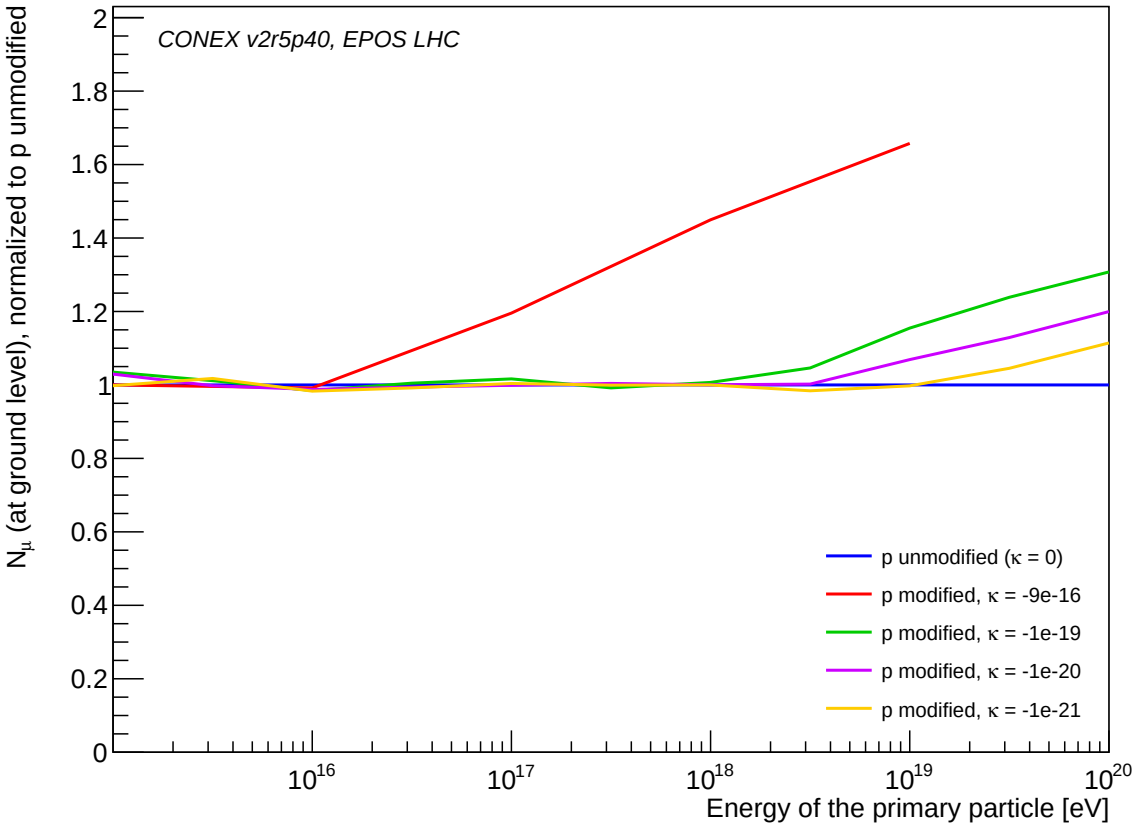

Figure 5.4.: *Average number of muons N_μ at ground level, normalized to the case of unmodified primary protons, in dependence of energy and κ.*

6. Analysis

The process of analyzing the MC simulations of the modified air shower simulation program CONEX is explained in this chapter.

Before the actual analysis can be done, the raw output of the CONEX code has to be reorganized so it is easier to access. This is done by an algorithm which bundles all the different .root-files of a single element for a certain value of κ produced by CONEX into one single .root-file.

6.1. Preparation of the CONEX Simulations

To consider the fact that the composition of cosmic rays is not a single type of primary particle, the results of the CONEX simulations for the four different elements with the same value of κ have to be mixed. The following steps are done for every possible mixture of elements:

First the sets of values for $X_{\max}$ of all four sets of simulations (proton, helium, oxygen, iron) are combined for each energy, using appropriate weigths corresponding to the portion of the respective element in the combination. If the combination consists of e. g. only 100 % protons, then the weight of every $X_{\max}$ value from proton simulations is set to 1, while all other weights are 0. Given the same number of points for all four elements and a target composition of 50 % proton, 25 % helium, 25 % oxygen and 0 % iron, the weights for the points of the different elements are 0.5, 0.25, 0.25 and 0.0 respectively. While the number of simulations for all elements should be the same (in this case 2000 entries per κ, element and energy bin) this is not guaranteed because of the possibility that CONEX simulations fail to complete. These jobs are usually rerun, but nevertheless the possibilty of a difference in the number of simulated events due to incomplete simulations should not be dismissed. Because of this, fluctuations of the number of datapoints have to be accounted for in the determination of the weights for each $X_{\max}$. The number of entries (n_{p}) for the proton in relation to the number of entries of the other element ($n_{\mathrm{He/O/Fe}}$) is used to modify the

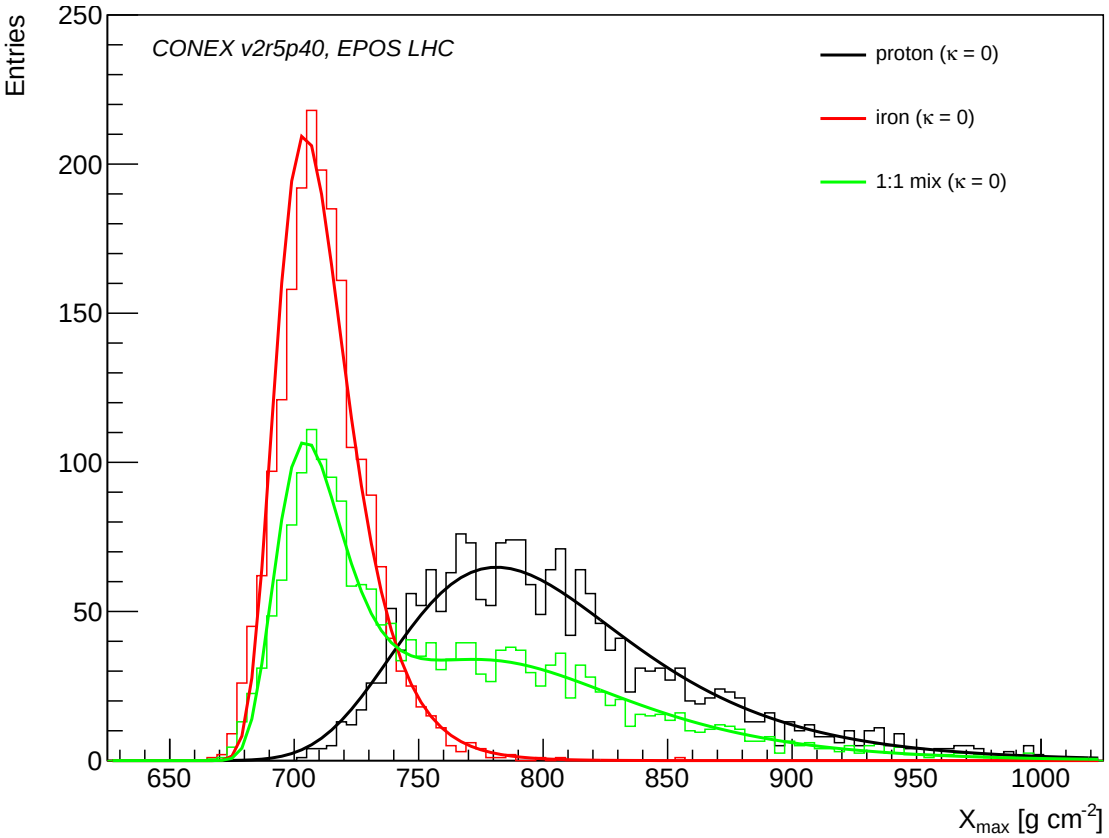

Figure 6.1.: *The distribution of X_{max}-values for protons, iron and a mixture of 50 % protons and 50 % iron. Protons as well as iron were simulated with $\kappa = 0$ (SM). The energy of the primary particle in both cases was $E_{Hadron} = 1 \times 10^{19}$ eV. The histograms represent the X_{max}-values simulated by CONEX. The functions are the respective Gumbel-distributions, renormalized to the number of entries in the histograms.*

weights ($w_{\mathrm{He/O/Fe}}$) of the other entries. The modified weights ($w_{\mathrm{p}}, w_{\mathrm{He/O/Fe}}$) in relation to the target percentage ($t_{\mathrm{p}}, t_{\mathrm{He/O/Fe}}$) of the element are given by:

$$\begin{aligned} w_{\mathrm{p}} &= t_{\mathrm{p}} \\ w_{\mathrm{He/O/Fe}} &= t_{\mathrm{He/O/Fe}} \frac{n_{\mathrm{p}}}{n_{\mathrm{He/O/Fe}}} \end{aligned} \tag{6.1}$$

This modification also enables the combination of simulations during their production to gain preliminary results. Since only the average atmospheric depth of the shower maximum $\langle X_{\mathrm{max}} \rangle$ as well as its fluctuations $\sigma(X_{\mathrm{max}})$ and their statistical errors for each primary particle energy are needed, it is not necessary to save the entire distribution of X_{max} values. Instead, only the values of $\langle X_{\mathrm{max}} \rangle$, $\sigma(\langle X_{\mathrm{max}} \rangle)$, $\sigma(X_{\mathrm{max}})$ and $\sigma(\sigma(X_{\mathrm{max}}))$ are saved.

The mixing of the different elements has various effects on the values of $\langle X_{\mathrm{max}} \rangle$ and $\sigma(X_{\mathrm{max}})$. The value of $\langle X_{\mathrm{max}} \rangle$ for a combination of elements is just the weighted mean

of the different $\langle X_{\max} \rangle$-values of the different elements, since it is only the mean value of all data points. The dependency of $\sigma(X_{\max})$ on the different weights of the elements is more complicated, since $\sigma(X_{\max})$ corresponds to the spread of the whole distribution of $X_{\max}$ values. One example for the differences between the $X_{\max}$ distributions of protons and iron as well as a proton-iron mix can be seen in Fig. 6.1.

The distributions for single elements are always asymmetrically clustered around a mean value and can be represented by a Gumbel distribution [31]:

$$f(x) = \frac{1}{\beta} \exp(-\frac{1}{\beta}(x-\mu)) \exp(-\exp(-\frac{1}{\beta}(x-\mu))) \tag{6.2}$$

With the parameters β and μ having the following relation to the expected value E and standard deviation σ of the distribution:

$$\begin{aligned} \beta &= \sigma \frac{\sqrt{6}}{\pi} \\ \mu &= E - \beta\gamma \end{aligned} \tag{6.3}$$

The parameter $\gamma \approx 0.5772$ is the Euler-Mascheroni constant. This approximation of the simulated $X_{\max}$-values by means of Gumbel functions can also work for a combination of two elements. The results of the combination of Fig. 6.1 were compared to the sum of two corresponding gumbel functions. The values of $\langle X_{\max} \rangle$ and $\sigma(X_{\max})$ gained using the combined set of proton and iron simulations match the values determined using the gumbel functions very well: Because of the different mean values $\langle X_{\max} \rangle$ of individual elements,

$\langle X_{\max} \rangle_{\text{Sim}} = 759.264\,\text{g}\,\text{cm}^{-2}$	$\sigma(X_{\max})_{\text{Sim}} = 62.7405\,\text{g}\,\text{cm}^{-2}$
$\langle X_{\max} \rangle_{\text{Gumbel}} = 759.163\,\text{g}\,\text{cm}^{-2}$	$\sigma(X_{\max})_{\text{Gumbel}} = 62.4663\,\text{g}\,\text{cm}^{-2}$

assuming a mix of different primary particles results in a combination of several overlapping distributions centered around different points. Depending on the distance between the distributions, the value of $\sigma(X_{\max})$ for the mix can be significantly larger than the values of $\sigma(X_{\max})$ for any sole element in the mix. One example for this effect can be seen in Fig. 6.2.

To validate the process of mixing the elements, a cross check is done to verify that the value of $\langle X_{\max} \rangle$ for a pure element is not changed after being processed. For this purpose, only 'pure' states, consisting to 100 % of one element, from the combined data set are taken and their $\langle X_{\max} \rangle$ are compared to the values derived directly from the CONEX data. If the process of combining the elements indeed does not change the data for pure combinations, as it should, no difference is generated between both values. The comparison between the original values and the values of $\langle X_{\max} \rangle$ after processing can be seen in Fig. 6.3. It is obvious that the value of $\langle X_{\max} \rangle$ does not differ between both cases. So it is verified that the algorithm works for single elements.

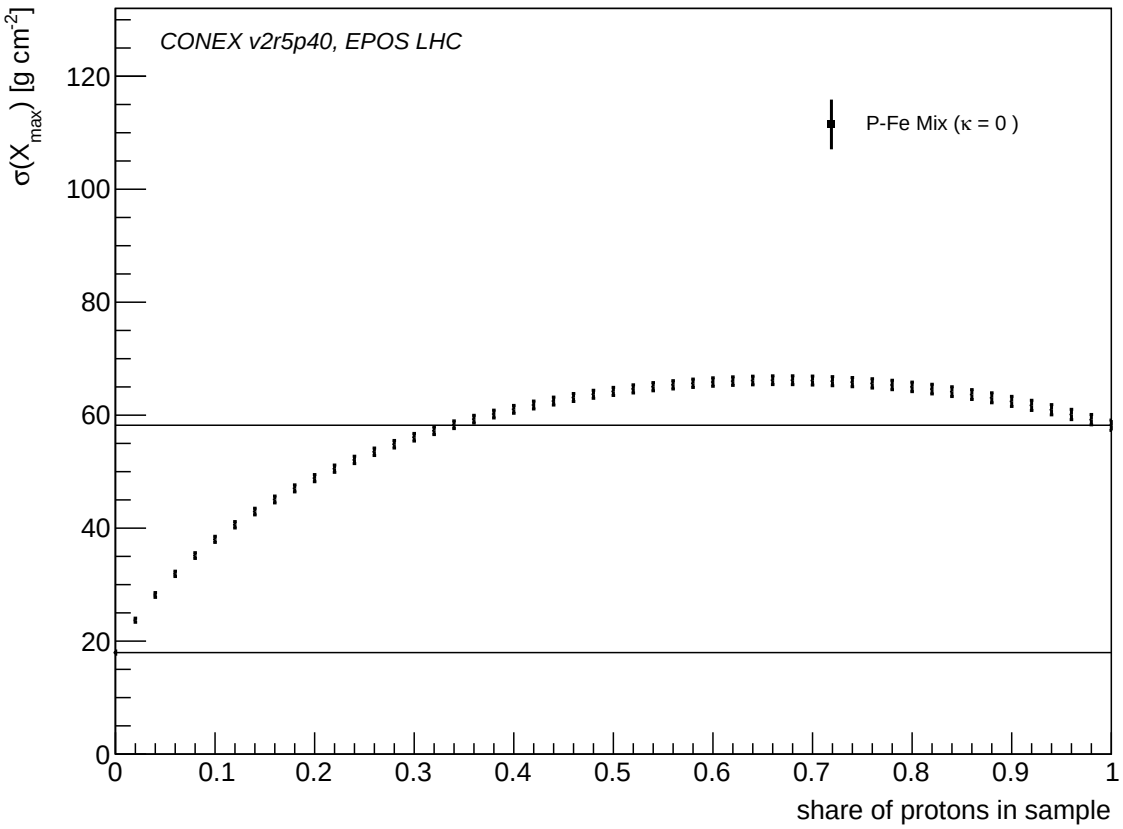

Figure 6.2.: *$\sigma(X_{max})$ of a combination of protons and iron as primary particles, in dependence of the fraction of protons in the combination. Both protons and iron were simulated with $\kappa = 0$ (SM). The primary energy is in both cases $E_{Hadron} = 1 \times 10^{19}\,\mathrm{eV}$.*

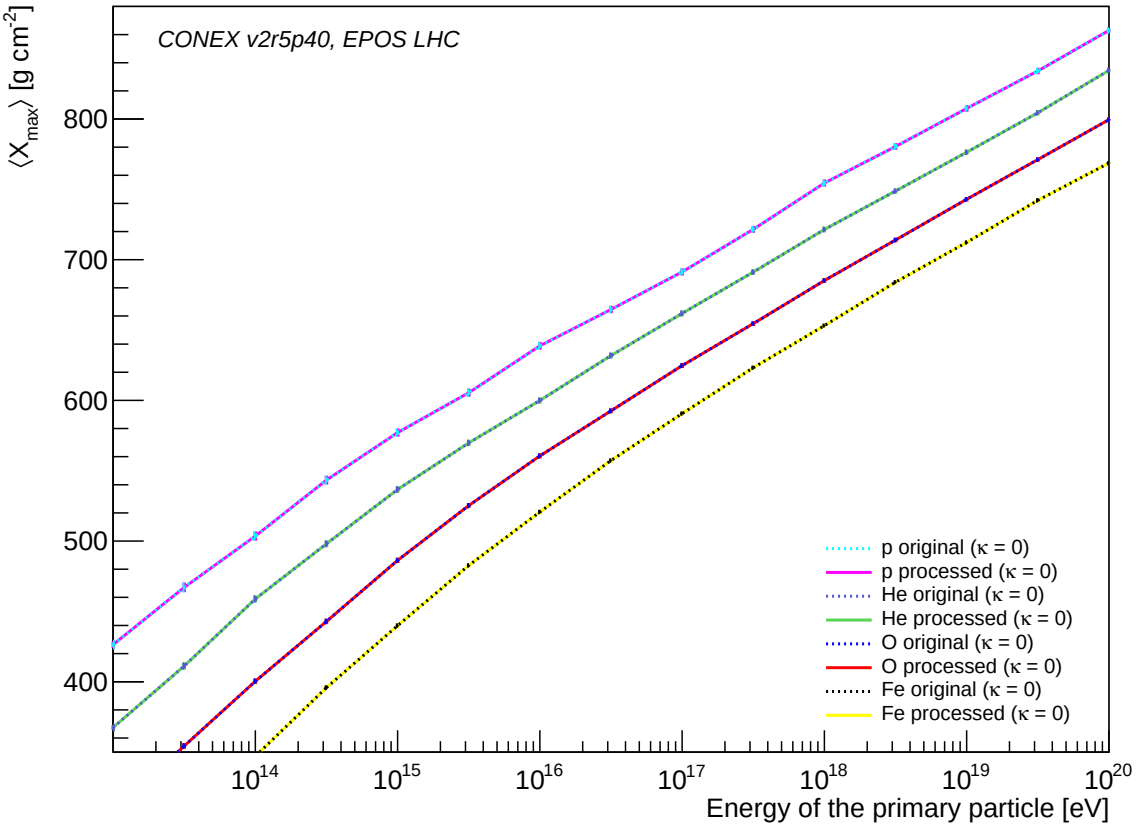

Figure 6.3.: *Comparison of $\langle X_{max} \rangle$ derived from original data and from the processed data set for single elements. Both protons and iron were simulated with $\kappa = 0$ (SM). It can clearly be seen that the values of $\langle X_{max} \rangle$ do not change due to the process of combination.*

6.2. Analysis under the Assumption of a Pure Proton Composition

The combined sets of CONEX simulations can now be analyzed. The first step is replicating the results gained in [1], using only proton-induced air showers simulated by CONEX and only comparing the values of $\langle X_{\max} \rangle$. In this segment, only a direct comparison between airshowers simulated with CONEX and experimental air shower data will be made to determine a bound on κ, not a parametrisation as used in [1], therefors the results should be similar, but do not have to match exactly. All the measurements used are from the Pierre Auger Observatory [4].

The results from the Pierre Auger observatory used in this section are based on data collected between the 1st of December 2004 to the 31st of December 2012, which corresponds to 19759 independent air shower events. The events used were reconstructed through a hybrid method using data from both the FD and the SD. Several selection cuts were applied to eliminate e. g. events of poor quality and air showers largely outside of the field of view of the FD. The first two moments of the $X_{\max}$ distributions of the measured air showers, $\langle X_{\max} \rangle$ and $\sigma(X_{\max})$, are then used to describe the main features of the distribution.

The direct comparison between Auger data published in 2014 and the values of $\langle X_{\max} \rangle$ for simulated proton induced air showers using different values of κ is presented in Figs. 6.4 and 6.5.

For each data point of the Auger data, it is tested if the simulations and the Auger data match. If the values of $\langle X_{\max} \rangle$ do not match for one of the energy values, the simulation does not match the experimental data. The numerical values between which the $\langle X_{\max} \rangle$ values of the simulations are considered to match the Auger data are determined considering the given uncertainties of the datapoints at 98% Confidence Level (CL). This is the same CL as used in [1] and [2], which will be maintained to simplify the comparison of the results.
The uncertainties taken into consideration are the statistical and systematic uncertainties of the Auger data set, as well as an additional systematic uncertainty arising from the choice of the hadronic interaction model. The uncertainty of $\langle X_{\max} \rangle$ due to the different models of hadronic interaction is about $\pm 20\,\mathrm{g\,cm^{-2}}$ around the value of EPOS LHC [28]. The predictions from the alternative models QGSJET-II-04 [29] and SIBYLL 2.3c [32] could also be considered, eliminating the need for the uncertainty on the predictions of

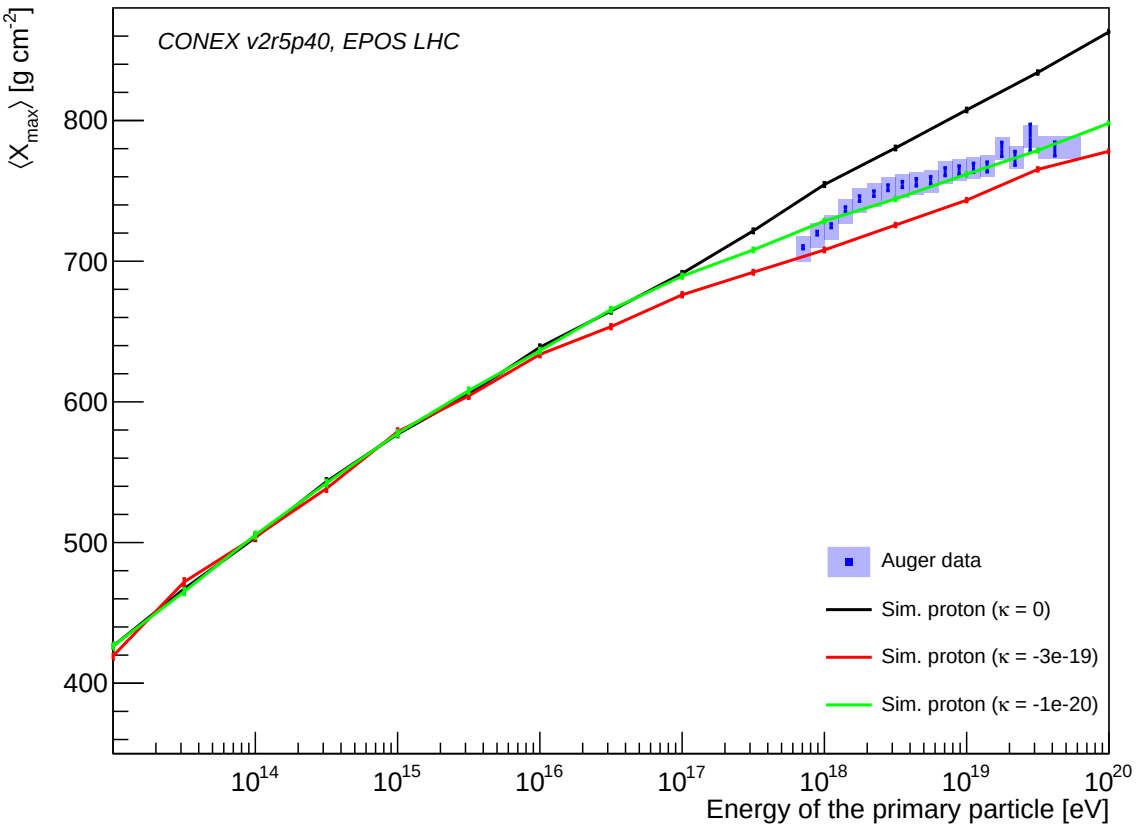

Figure 6.4.: *Comparison of $\langle X_{max} \rangle$ values derived from simulated proton induced air showers and Auger data (2014) [4].*

EPOS LHC. Here, however, only the EPOS LHC model is used and a systematic uncertainty of $\pm 20\,\mathrm{g\,cm^{-2}}$ is applied.

The values of $\langle X_{\mathrm{max}} \rangle$ for which the simulated air showers are considered to match the Auger data are determined by taking the experimental value and using MC simulations to simulate the effects of the different uncertainties on it. The statistical uncertainty is simulated by moving the Auger value by a random amount, drawn from a gaussian distribution with the width of the statistical error. For the systematic errors a similar method is applied, but the distributions from which the values are drawn are uniform, not gaussian. The repetition of this process produces a distribution of $\langle X_{\mathrm{max}} \rangle$ values, from which the accepted values of $\langle X_{\mathrm{max}} \rangle$ can be determined. For the analysis done in this thesis a two-sided Confidence Interval (CI) is computed, corresponding to a CL of 96 %. An example for this kind of distribution is Fig. 6.6, the original value of $\langle X_{\mathrm{max}} \rangle$ as well as the borders of the CI are marked. It is worth noting that, even though the systematic uncertainty of the model $\sigma_{\mathrm{Sys,Model}} = 20\,\mathrm{g\,cm^{-2}}$ is an uncertainty of the simulation, not of the Auger data, it is still applied to the value obtained by Auger. The main reason for this is practicality. Using this method, the CI has to be computed only once for each energy value, doing a

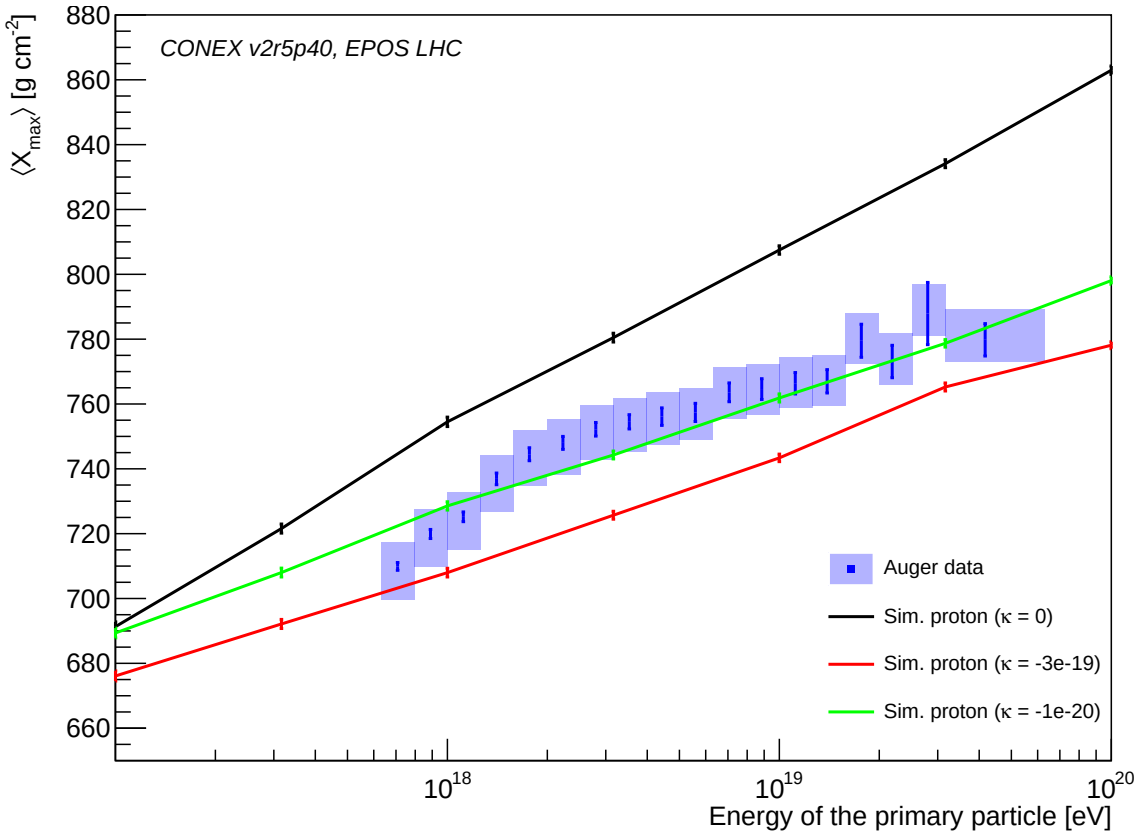

Figure 6.5.: *Comparison of $\langle X_{max} \rangle$ values derived from simulated proton induced air showers and Auger data (2014) [4] with a decreased range in energy and $\langle X_{max} \rangle$ for a closer look at the region relevant to the analysis.*

MC simulation for each simulated event would take much longer (approximately ten times longer for one element and 50,000 times longer for the combinations discussed later).

Since the value of $\langle X_{\mathrm{max}} \rangle$ of unmodified CONEX simulations is above the Auger data in all cases, only the lower border of the CI is used in this section to determine if a certain value of κ is allowed. Therefore, the used CI becomes one-sided with a corresponding CL of 96 %, the same CL that was used in [1]. This is done due to the fact that $\langle X_{\mathrm{max}} \rangle$ is larger for lighter primary hadrons, which means any composition other than pure protons has a smaller value of $\langle X_{\mathrm{max}} \rangle$. If the highest possible $\langle X_{\mathrm{max}} \rangle$ value for a certain κ is lower than the lower bound of allowed $\langle X_{\mathrm{max}} \rangle$ values according to the Auger data, then it can safely be concluded that the κ value should be excluded. The upper border of the CI will not be used here, but the same method will be used later, using the two-sided CI.

Since the energy values of the data points given by Auger are not the same ones used in the CONEX simulations, an extrapolation has to be used. This is less accurate than simulating data sets for each energy in the Auger data set, but saves a lot of computing

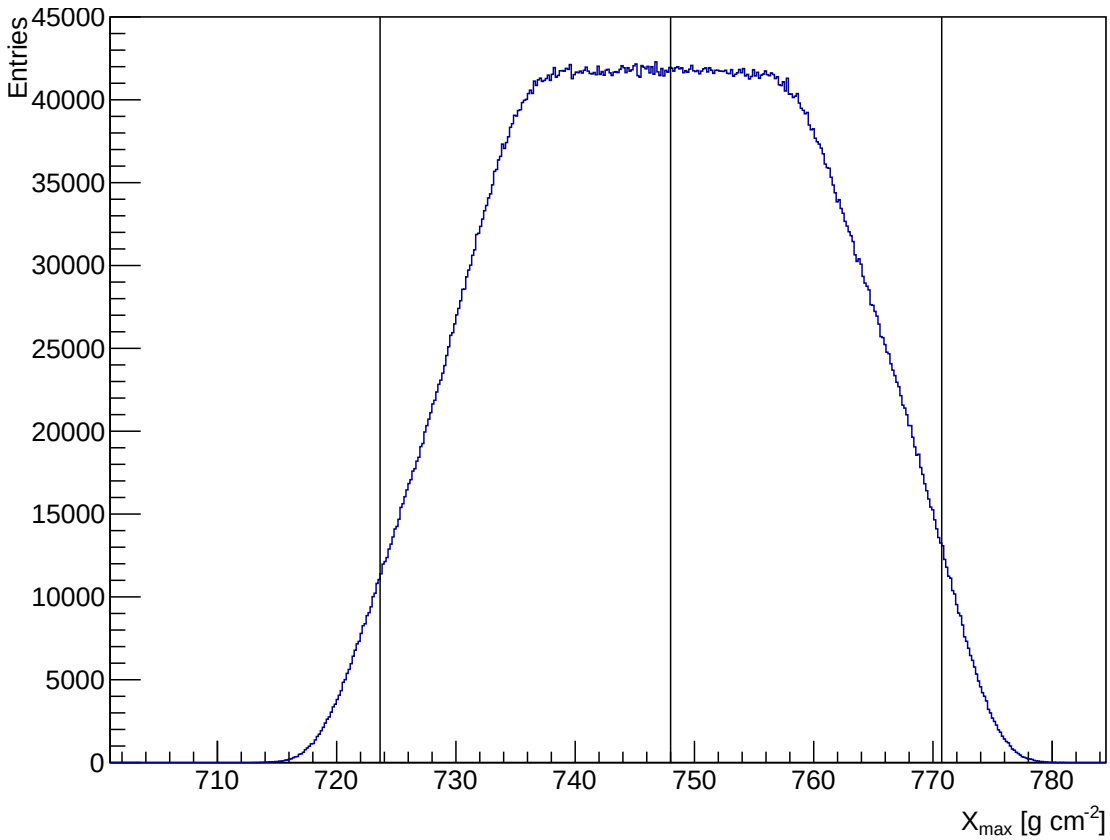

Figure 6.6.: *The full Sample of a MC simulation of the uncertainties of* $\langle X_{max} \rangle$ *for an actual Auger data entry. The values used are:* $\langle X_{max} \rangle = 748\,\mathrm{g\,cm^{-2}}$, $\sigma_{Stat} = 2\,\mathrm{g\,cm^{-2}}$, $\sigma_{Sys,Up} = 7.3\,\mathrm{g\,cm^{-2}}$, $\sigma_{Sys,Low} = -9.4\,\mathrm{g\,cm^{-2}}$. *In Addition to this a model error of* $\sigma_{Sys,Model} = 20\,\mathrm{g\,cm^{-2}}$ *is assumed and the upper and lower borders of the CI are set at* $2\,\%$ *of the sample data. The computed upper and lower borders of the possible values of* $\langle X_{max} \rangle$, *as well as the original* $\langle X_{max} \rangle$ *value are marked in the histogram by vertical lines.*

time, especially since the energy bins of the Auger data from different years differ. The change in $\langle X_{\mathrm{max}} \rangle$ as well as in $\sigma(X_{\mathrm{max}})$ resulting from a different energy of the primary hadrons are both smooth and monotonous, so a linear approximation between simulated data points is used. In praxis this is done by determining the weighted mean of the values at the CONEX data points next to the Auger data point on the energy scale, the relative weights are determined by the relative position of the Auger data point between them

on the logarithmic scale. One example for such weighting is given below for one energy bin:

$$\begin{aligned}
\text{CONEX results:}\quad & E_{\mathrm{C},1} = 10^{19}\mathrm{eV} \;\; \langle X_{\max}\rangle_{\mathrm{C},1} = 788.409\,\mathrm{g\,cm^{-2}} \\
& E_{\mathrm{C},2} = 10^{19.5}\mathrm{eV} \;\; \langle X_{\max}\rangle_{\mathrm{C},2} = 805.474\,\mathrm{g\,cm^{-2}} \\
\text{Auger data:}\quad & E_{\mathrm{A}} = 10^{19.05}\,\mathrm{eV} \\
\text{Weight:}\quad & p = 0.9 \\
\text{Result:}\quad & E_{\mathrm{C,comb}} = 10^{p\times 19+(1-p)\times 19.5}\mathrm{eV} = 10^{19.05}\,\mathrm{eV} \\
& \langle X_{\max}\rangle_{\mathrm{C,comb}} = (p\times 788.409 + (1-p)\times 805.474)\mathrm{g\ cm^{-2}} \\
& = 790.116\,\mathrm{g\,cm^{-2}}
\end{aligned} \tag{6.4}$$

The weighted result can be compared to the Auger data. Contrary to all other energy bins, which span a range of 0.1 in $log_{10}(E)$, the last energy bin ($E_{\mathrm{Hadron}} = 10^{19.62}$eV) of the Auger data has no upper energy limit. The large energy span of this bin makes the values of the parameters derived from this energy not comparable to the CONEX simulations, which are done at one singular energy value each. This fact as well as the large uncertainties of the parameters for this energy are the root cause for not using this energy bin in the later analysis to set any limits, although the results are still displayed.

This test was done for several values of κ and the corresponding results can be seen in Tab. 6.1. In order for a κ-value to be rejected, it is sufficient that only one energy bin of this value has a simulated $\langle X_{\max}\rangle$ lower than the experimental lower bound. This is the case for $\kappa = -4\times10^{-19}$, $\kappa = -3\times10^{-19}$ and $\kappa = -2\times10^{-19}$ but not the case for all values of $\kappa \geq -1\times10^{-19}$ (see Tab. 6.1).

This sets the first limit at $\kappa > -2\times10^{-19}$ since this is the value closest to zero which can be excluded. In [1] the bound is given as $\kappa > -3\times10^{-19}$, which would be the neighboring data point in this analysis.

$log_{10}(E_{\text{Hadron}}[\text{eV}])$	Accepted for				
	$\kappa = -4 \times 10^{-19}$	$\kappa = -3 \times 10^{-19}$	$\kappa = -2 \times 10^{-19}$	$\kappa = -1 \times 10^{-19}$	$\kappa = -1 \times 10^{-20}$
17.85	1	1	1	1	1
17.949	1	1	1	1	1
18.048	1	1	1	1	1
18.148	1	1	1	1	1
18.247	0	0	1	1	1
18.348	0	0	0	1	1
18.447	0	0	0	1	1
18.548	0	0	1	1	1
18.646	0	0	1	1	1
18.747	1	1	1	1	1
18.849	0	0	1	1	1
18.947	1	1	1	1	1
19.048	1	1	1	1	1
19.144	1	1	1	1	1
19.247	0	1	1	1	1
19.34	1	1	1	1	1
19.447	1	1	1	1	1
19.62	1	1	1	1	1

Table 6.1.: *Result of the $\langle X_{max} \rangle$ analysis for protons. For each value of E_{Hadron} and κ it can be seen if the $\langle X_{max} \rangle$ results of the modified simulation matches the Auger Data. The largest LV which still matches the Auger Data in all energy bins is $\kappa = -1 \times 10^{-19}$.*

The shower fluctuations $\sigma(X_{\max})$ are another shower observable which can be used to determine if the simulated air showers correspond to the Auger data. The direct comparison between the CONEX simulations and the observations made by Auger is displayed in Fig. 6.7. It should be noted that the LV modifications leave $\sigma(X_{\max})$ essentially unchanged, in contradiction the behaviour of $\langle X_{\max} \rangle$. Since the behaviour of $\sigma(X_{\max})$ is independent from the value of κ, it cannot be of any use in the case of a pure proton composition as primary particles to determine any bound on κ. But it can be used to determine if the assumption of a certain composition of primary particles, in this case only protons, is reasonable. By just looking at the graphs in Fig. 6.7 it can be seen that a pure proton hypothesis matches the Auger data reasonably well in the regions of lower energies ($E < 10^{18.5}$eV). But at higher energies there are significant differences between $\sigma(X_{\max})$ in simulations and Auger data. This suggests a shift to heavier primary particles with a rise in the energy of the primary hadrons. A more in-depth analysis of this parameter and how it can be used to improve the bounds on κ is done in Sec. 6.3.

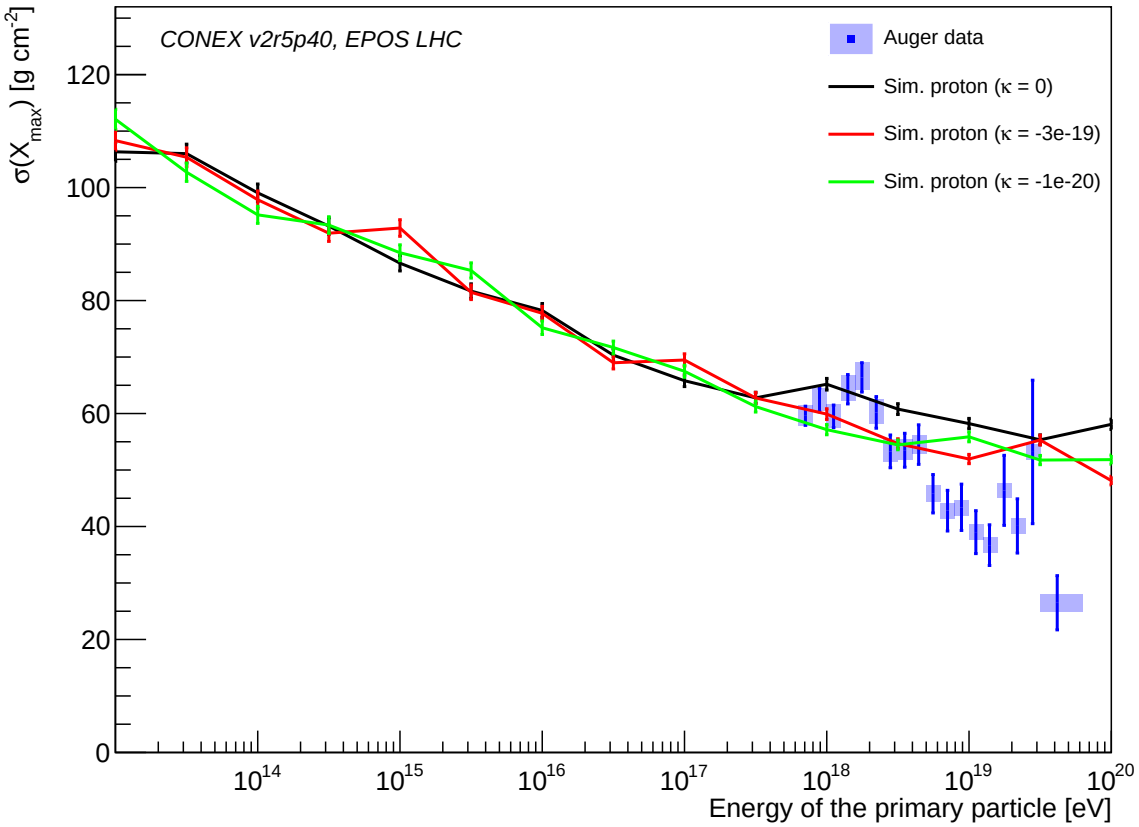

Figure 6.7.: *Comparison of $\sigma(X_{max})$ values derived from simulated proton induced air showers and Auger data (2014) [4]. It can be seen that the values of $\sigma(X_{max})$ do not differ significantly for different κ. The Auger data points overlap with the simulated proton values at energies below $1 \times 10^{18.5}$ eV, above this threshold the Auger $\sigma(X_{max})$ values are below the simulated ones.*

The same method as before is used to apply bounds on $\sigma(X_{\max})$, taking into account the mean value of it as well as the statistical and systematical uncertainties, but not adding an additional systematic error for the uncertainty of the model, since there is no scientific consensus on the systematic uncertainties due to the choice of model. The result of this is that neither the modified simulations nor the unmodified simulation match the Auger data in $\sigma(X_{\max})$ in all energy bins. For unmodified protons, the simulated values are above the experimental bounds at energies around $1 \times 10^{18.05}\,\mathrm{eV}$, while they are below at energies around $1 \times 10^{19}\,\mathrm{eV}$ (see also Fig. 6.7). The logical next step of allowing an additional element to be part of the simulated cosmic primary hadrons, which has the effect of lowering the value of $\langle X_{\max} \rangle$ and can change the value of $\sigma(X_{\max})$ in both directions depending on the proportion of elements is explored in the following section.

6.3. Analysis under the Assumption of a Proton and Iron Combination

The next step is to explore the possibility of a mix of two elements to test the effects of assuming a combination of primary elements. Protons and iron nuclei are chosen, to cover both extreme ends of the possible mass scale. The shower observable $\sigma(X_{\max})$ can be used here as a second parameter in the analysis to test whether a certain combination of elements agrees with the Auger data. From this, an expansion of the analysis follows to include both $\langle X_{\max} \rangle$ and $\sigma(X_{\max})$, as well as using all of the combined datasets derived from the raw CONEX output which include a proton-iron mixture only.

The Auger data set used here and in the following chapters is a newer one from 2017 [33] which includes the Auger measurements from three more years than the one used before, which was primarily used to ensure comparability to the bound set in [1]. The newer Auger data set includes measurements from the 1st of December 2004 to the 31st of December 2015and the energy range of the data set is also increased from a lower bound of $E > 10^{17.8}\,\text{eV}$ to $E > 10^{17.2}\,\text{eV}$ due to detector improvements. The total number of showers in the data sample is 42,622, more than double the value of the Auger data from 2004. To achieve the highest possible precicion, the later statistics with the higher number of entries should be used.

The procedure described in Sec. 6.1 produces datasets which include combinations containing all four of the simulated elements. Here only those combinations which consist purely of protons and iron are taken into account. In Figs. 6.8 and 6.9, the values of $\langle X_{\max} \rangle$ and $\sigma(X_{\max})$ are displayed and compared to the Auger data from 2017. Several conclusions can be derived even without further analysis. Both $\langle X_{\max} \rangle$ and $\sigma(X_{\max})$ values are lower for iron than for protons and the statistical fluctuations are reduced, both in the SM simulation as well as those which include LV. The effect of LV on $\langle X_{\max} \rangle$ can be seen starting at higher energies for iron than for protons, the difference is a factor of approximately 30. This is due to the lower energy per nucleon of an iron nucleus compared to a proton of the same energy (iron consists of 56 nucleons, a proton only of one). In the superposition model used in the CONEX simulations, the iron nucleus is treated as 56 protons which each have an energy of $\frac{1}{56}$ of the iron nucleus, which leads to a lower energy of photons in the iron-induced air shower. Since the energy threshold given in (2.7) needs to be reached by photons to have any impact of LV on the simulation this leads to a shift of the effect to higher energies for heavier primary particles. As with the proton before, no change in $\sigma(X_{\max})$ is noticed for iron due to the introduction of LV. The values of $\sigma(X_{\max})$ for iron are much lower than those for protons, again due to the superposition model treating iron as 56 protons, thus reducing fluctuations. It should also

be noted that the uncertainties of the Auger data from 2017 are reduced compared to 2014.

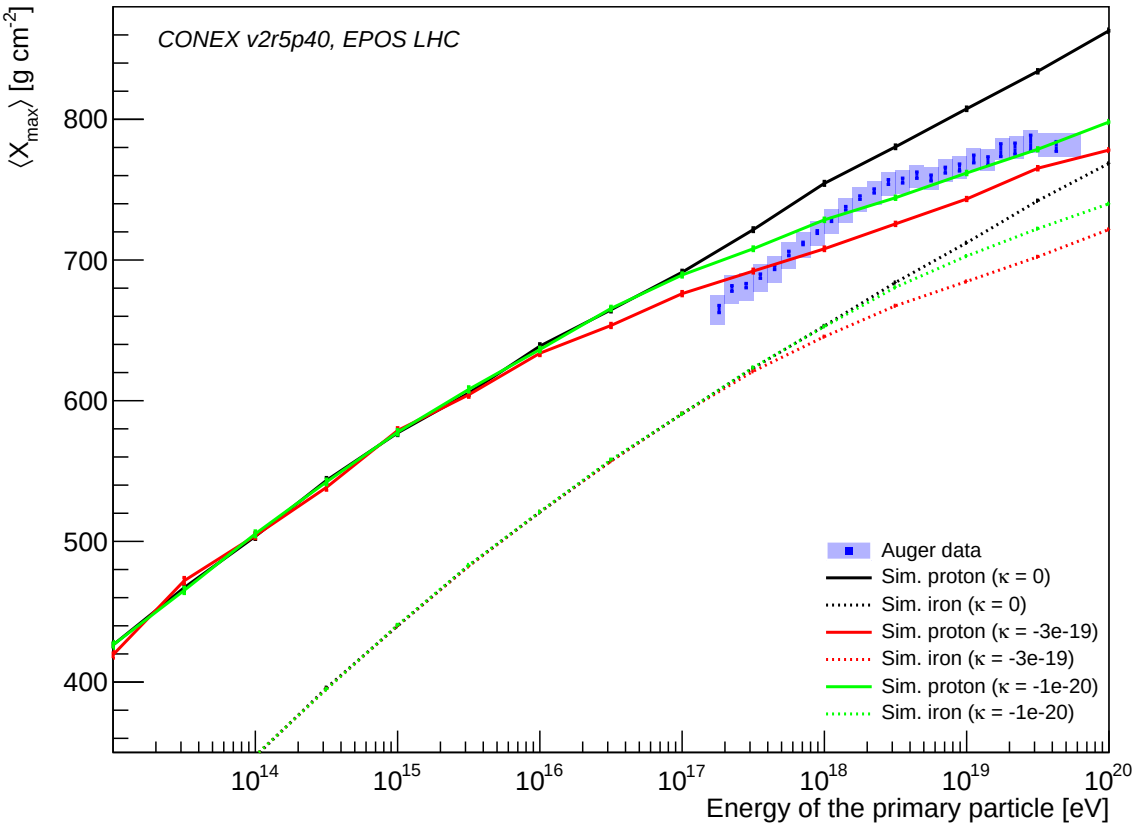

Figure 6.8.: *Comparison of $\langle X_{max} \rangle$ values derived from simulated proton or iron induced air showers and Auger data (2017) [33]. The values of $\langle X_{max} \rangle$ are much lower for iron nuclei than for protons, the effects of LV on $\langle X_{max} \rangle$ can be seen in iron starting at higher energies. In the unmodified simulations the Auger data points lie between the values of proton and iron, for more negative values of κ the Auger data points are above the simulated proton values of $\langle X_{max} \rangle$.*

The simulated air showers are compared to the measured Auger data as described in this section. The comparison is done for each energy bin seperately, both $\langle X_{\max} \rangle$ and $\sigma(X_{\max})$ are checked. A simulated energy value is considered matching the Auger data in one of the parameters if the simulated value lies inside the CI computed from the Auger data as described in Sec. 6.2. The number of possible combinations of primary particles which match the Auger data in both or one of the parameters are then noted for each energy at each value of κ. The difference in proton percentage between two neighboring combinations is 2 %, resulting in a maximum of 51 possible combinations for each energy and κ value. In Tab. 6.2, as well as in Tabs. A.1 and A.2 in the appendix, the number of accepted combinations for each value of the primary particle energy and κ is listed. From this table, the most important conclusion is, that for no value of κ (even $\kappa = 0$, corresponding to the SM) accepted combinations of primary hadrons exist for every energy bin.

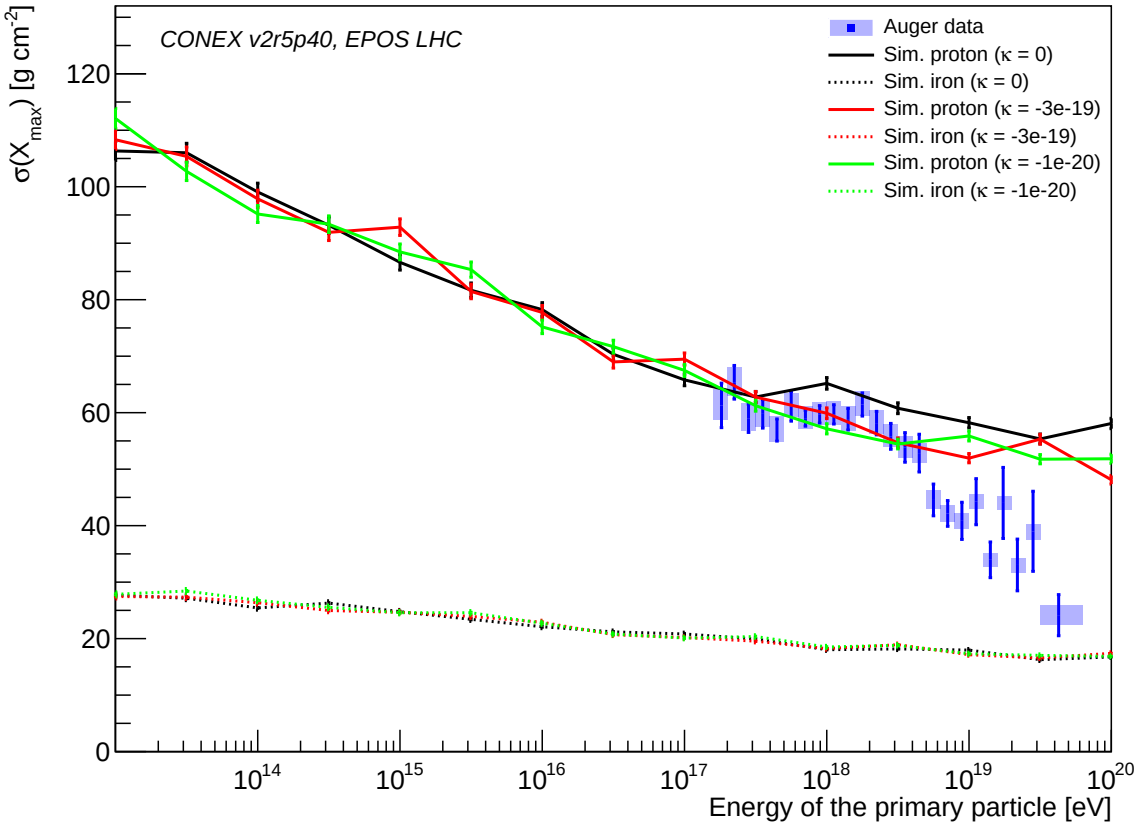

Figure 6.9.: *Comparison of $\sigma(X_{max})$ values derived from simulated proton or iron induced air showers and Auger data (2017) [33]. The values of $\sigma(X_{max})$ are much lower for iron nuclei than for protons, both do not change for different values of κ. All Auger data points are either at or between the simulated values for protons and iron.*

Therefore, the hypothesis of a combination of only protons and iron as primary hadrons at the entire energy spectrum has to be rejected. This does not exclude the possibility of combinations of proton and iron or even pure protons at some energy values, but at specific energies (i.e. around $E_{\mathrm{Hadron}} = 1 \times 10^{19}\,\mathrm{eV}$) this combination does not agree with Auger data.

$log_{10}(E_{\mathrm{Hadron}}[\mathrm{eV}])$	$\kappa = -3 \times 10^{-19}$			$\kappa = -1 \times 10^{-19}$			$\kappa = -3 \times 10^{-20}$			$\kappa = -1 \times 10^{-20}$		
	Accepted for			Accepted for			Accepted for			Accepted for		
	Both	$\langle X_{\mathrm{max}} \rangle$	$\sigma(X_{\mathrm{max}})$	Both	$\langle X_{\mathrm{max}} \rangle$	$\sigma(X_{\mathrm{max}})$	Both	$\langle X_{\mathrm{max}} \rangle$	$\sigma(X_{\mathrm{max}})$	Both	$\langle X_{\mathrm{max}} \rangle$	$\sigma(X_{\mathrm{max}})$
17.26	29	29	36	30	30	36	28	28	38	27	27	39
17.35	22	22	29	25	25	29	27	27	32	28	28	33
17.45	24	24	33	27	27	34	13	28	22	14	28	23
17.55	22	22	31	25	25	32	27	27	35	28	28	35
17.65	7	21	18	24	24	33	7	27	15	9	28	17
17.75	16	16	27	19	19	27	23	23	31	25	25	32
17.85	13	13	26	17	17	25	21	21	29	23	23	30
17.95	9	9	23	13	13	20	18	18	26	21	21	28
18.05	5	5	22	10	10	20	15	15	25	18	18	27
18.15	1	1	23	6	6	23	12	12	26	15	15	27
18.25	0	0	14	3	3	17	9	9	21	9	12	17
18.35	0	0	22	2	2	25	8	8	27	12	12	25
18.45	0	0	26	0	0	29	6	6	30	9	9	28
18.55	0	0	29	3	3	32	8	8	33	11	11	31
18.65	0	0	32	2	2	34	8	8	35	11	11	34
18.75	0	1	16	0	7	13	0	12	13	0	16	13
18.85	0	0	11	0	5	9	0	10	10	0	14	9
18.95	0	0	16	0	6	12	0	12	14	0	16	13
19.05	0	0	29	0	4	20	1	10	27	0	14	21
19.15	0	3	10	0	8	9	0	14	10	0	18	9
19.24	1	1	36	0	5	28	11	11	43	9	15	37
19.34	0	3	11	0	6	12	0	13	13	0	16	13
19.45	0	5	20	0	8	23	0	14	24	0	18	27
19.63	0	10	7	0	14	7	0	20	7	0	24	8

Table 6.2.: *Result of both the $\langle X_{max} \rangle$ and $\sigma(X_{max})$ analysis for all combinations of protons and iron. For each value of E_{Hadron} and κ the number of results of the modified simulation matching the Auger Data(2017) [33] are given. The simulated shower observables do not match the Auger Data in all energy bins for any κ value.*

6.4. Analysis under the Assumption of a Combination of four Primary Elements

To have access to a wider range of primary hadron masses the additional elements helium and oxygen are added to the list of simulated primary hadrons. Now each of the four elements is taken as representative for all elements surrounding it on the mass scale, since both $\langle X_{\mathrm{max}} \rangle$ and $\sigma(X_{\mathrm{max}})$ depend mainly on mass. For example for nitrogen ($m = 14\,\mathrm{u}$) and oxygen ($m = 16\,\mathrm{u}$) no great differences are expected in both parameters. The stepsize between the combinations is again taken as $2\,\%$, the higher number of possiblbe primary hadrons in the combinations leads to an exponential increase in possibilites. The total number of possible primary hadron combinations has thus been increased to 23,426.

The same process as in Sec. 6.3 is done to analyze the data: For each point of data of the Auger measurements the CIs are determined, inside of which $\langle X_{\mathrm{max}} \rangle$ and $\sigma(X_{\mathrm{max}})$ values are accepted, then the combined CONEX data sets are compared to these. The numbers of accepted primary hadron combinations for two values of κ and all energies can be seen in Tab. 6.3, the complete Tabs. A.3 to A.5 are presented in the appendix.

At the previous bound $\kappa \geq -3 \times 10^{-19}$, the values of the simulations and the Auger data do not match. There is no combination of elements where simulations and data fit for both parameters above an energy of $10^{18.2}\,\mathrm{eV}$, except at $E_{\mathrm{Hadron}} = 10^{19.24}\,\mathrm{eV}$. This is mainly due to heavier compositions being accepted in the $\sigma(X_{\mathrm{max}})$-channel and lighter compositions being accepted due to $\langle X_{\mathrm{max}} \rangle$, as can be seen later in Figs. 6.10 and 6.12.

By also considering κ values closer to zero the observations described in the following paragraphs can be made. For all values of κ and all primary hadron energies, there are combinations where the $\sigma(X_{\mathrm{max}})$ Auger data matches the simulated showers . Since $\sigma(X_{\mathrm{max}})$ is mostly independent of κ and the experimental values of $\sigma(X_{\mathrm{max}})$ are either compatible with a pure proton assumption (low E_{Hadron}) or are set between the values for simulated protons and iron, thus guaranteeing a possible combination, this is not surprising.

$log_{10}(E_{\text{Hadron}}[\text{eV}])$	$\kappa = -3 \times 10^{-19}$			$\kappa = -5 \times 10^{-20}$			$\kappa = -3 \times 10^{-20}$		
	Accepted for			Accepted for			Accepted for		
	Both	$\langle X_{\text{max}} \rangle$	$\sigma(X_{\text{max}})$	Both	$\langle X_{\text{max}} \rangle$	$\sigma(X_{\text{max}})$	Both	$\langle X_{\text{max}} \rangle$	$\sigma(X_{\text{max}})$
17.26	8396	16717	8729	8459	18782	8622	9872	18950	10231
17.35	2640	9999	2799	2182	13409	2228	3666	14251	3822
17.45	5430	11492	6090	5802	15098	6116	7496	15948	8021
17.55	4020	9699	4532	4371	13919	4580	6044	15007	6423
17.65	4368	8200	5470	5274	13030	5738	6350	14246	6959
17.75	1857	4065	2522	2299	9292	2516	3098	10748	3400
17.85	1249	2302	2004	1735	7287	1963	2156	8738	2409
17.95	604	905	1314	1064	5012	1259	1151	6290	1315
18.05	170	178	1117	801	2672	1154	891	3631	1182
18.15	6	6	1331	727	1159	1667	961	1728	1911
18.25	0	0	95	111	433	272	282	733	599
18.35	0	0	971	269	286	1722	491	530	2441
18.45	0	0	2249	99	99	3384	209	209	4409
18.55	0	0	4073	246	246	5413	493	493	6303
18.65	0	0	6291	236	236	7592	439	439	7981
18.75	0	1	14456	83	973	12976	398	1610	13330
18.85	0	0	13072	0	586	11379	14	1012	12056
18.95	0	0	16980	1	885	15055	175	1436	16229
19.05	0	0	17993	140	456	17195	777	816	17683
19.15	0	34	11025	0	1355	10965	1	2286	11477
19.24	2	2	20496	622	622	20027	1219	1219	20133
19.34	0	34	12830	0	922	14393	5	1808	14208
19.45	0	133	20428	863	1263	22162	1754	2486	21867
19.63	0	900	2542	0	4148	3225	0	6459	2901

Table 6.3.: *Result of both the $\langle X_{max} \rangle$ and $\sigma(X_{max})$ analysis for all combinations of all four elements. For each value of E_{Hadron} and κ the number of results of the modified simulation matching the Auger Data (2017) [33] can be seen. The simulated shower observables match the Auger Data in all energy bins only for $\kappa \geq -3 \times 10^{-20}$.*

At $\kappa \leq -1 \times 10^{-19}$ there is no combination of simulated elements that fits the experimental value of $\langle X_{\mathrm{max}} \rangle$ at energies around $E_{\mathrm{Hadron}} = 10^{18.45}\,\mathrm{eV}$. Looking at Fig. 6.8 it can be seen that the Auger $\langle X_{\mathrm{max}} \rangle$ value at this energy is the highest relative to the results of the CONEX simulation. Since the $\langle X_{\mathrm{max}} \rangle$ value decreases with lower values of κ, there is a certain value of κ below which no combination of elements can reach the lower bound set by the Auger data. The lowest κ for which all energies have valid combinations of elements matching the Auger data in both $\langle X_{\mathrm{max}} \rangle$ and $\sigma(X_{\mathrm{max}})$ is $\kappa = -3 \times 10^{-20}$. The last energy bin, where still no match between data and simulations is found, is ignored for this analysis, since the values are not reliable for reasons explained in Sec. 6.2. The highest value of κ which can be excluded is the last one where no match between data and simulations is found, leading to a new lower bound of

$$\kappa \geq -5 \times 10^{-20}. \tag{6.5}$$

The most important energy bins in setting this new bound are $E_{\mathrm{Hadron}} = 1 \times 10^{19.15}\,\mathrm{eV}$ and $E_{\mathrm{Hadron}} = 1 \times 10^{19.34}\,\mathrm{eV}$ where at a value of $\kappa = -3 \times 10^{-20}$ one or five combinations, respectively, are accepted, while at $\kappa = -1 \times 10^{-19}$ there are none. Both in $\langle X_{\mathrm{max}} \rangle$ as well as in $\sigma(X_{\mathrm{max}})$ there are many combinations of simulated primary hadrons which match the Auger data, so analyzing which specific combinations are accepted or rejected can lead to a better understanding of how the bounds are created. In Figs. 6.10 and 6.12 all possible combinations are shown for one energy value at two different values of κ.

The only difference between the figures is the value of κ used by the modified CONEX code, which can be used to make qualitative claims about the changes in accepted combinations of primary hadrons between different κ values. More examples (including Figs. 6.10 and 6.12) can be found in the appendix in Figs. B.1 to B.6. One first observation is that the combinations which match in $\sigma(X_{\mathrm{max}})$ do not change visibly with a change in κ, which is expected, since the simulated shower fluctuations remain mostly unchanged under LV modifications. The combinations which match the Auger data in $\langle X_{\mathrm{max}} \rangle$ increase in number with κ-values getting closer to zero. For both parameters, the combinations which are accepted are not lone points, but regions with percievable boundaries exist in the phase-space of possible combinations, where the combinations are accepted compared to $\langle X_{\mathrm{max}} \rangle$ or $\sigma(X_{\mathrm{max}})$ of the Auger data. Where those regions overlap, there are combinations which are accepted both in $\langle X_{\mathrm{max}} \rangle$ and $\sigma(X_{\mathrm{max}})$ (see Figs. 6.10 and 6.11). If for a certain κ-value there is such an overlap for all energy bins of the Auger data, this value matches the data and it follows that it has to be closer to zero than the established bound. Since both phase spaces change countinously with changing κ it seems possible to use this to set more precise bounds on κ through interpolation between simulated data points. Without exact calculation the change of the regions with κ can only be approximated. Qualitatively it can be assumed by looking at Figs. 6.10 and 6.12 that the actual limit, if

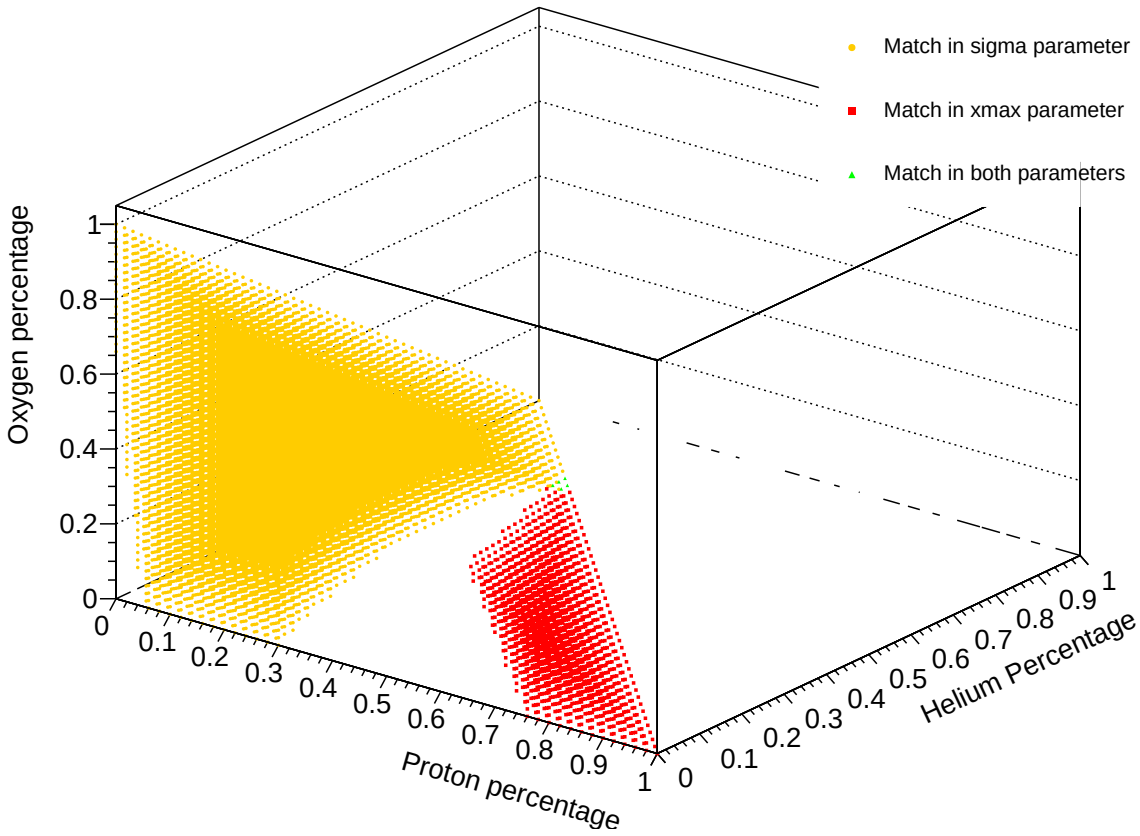

Figure 6.10.: *Visual representation of all possible combinations of simulated protons, helium, oxygen and iron which correspond to the Auger data(2017) [33] in either* $\langle X_{max} \rangle$*,* $\sigma(X_{max})$ *or both. The value of* κ *used for the simulations is* -3×10^{-20}*. The Auger data compared to is the energy bin* $E_{Hadron} = 1 \times 10^{19.34}\,\mathrm{eV}$*.*

we were not limited by a finite statistic, would be between the values of $\kappa = -5 \times 10^{-20}$ and $\kappa = -3 \times 10^{-20}$ while being closer to $\kappa = -3 \times 10^{-20}$. However without detailed calculations this is just an educated guess, which is why the actual limit gained by comparing the simulations to Auger data remains as $\kappa = -5 \times 10^{-20}$, being the excluded κ value closest to zero.

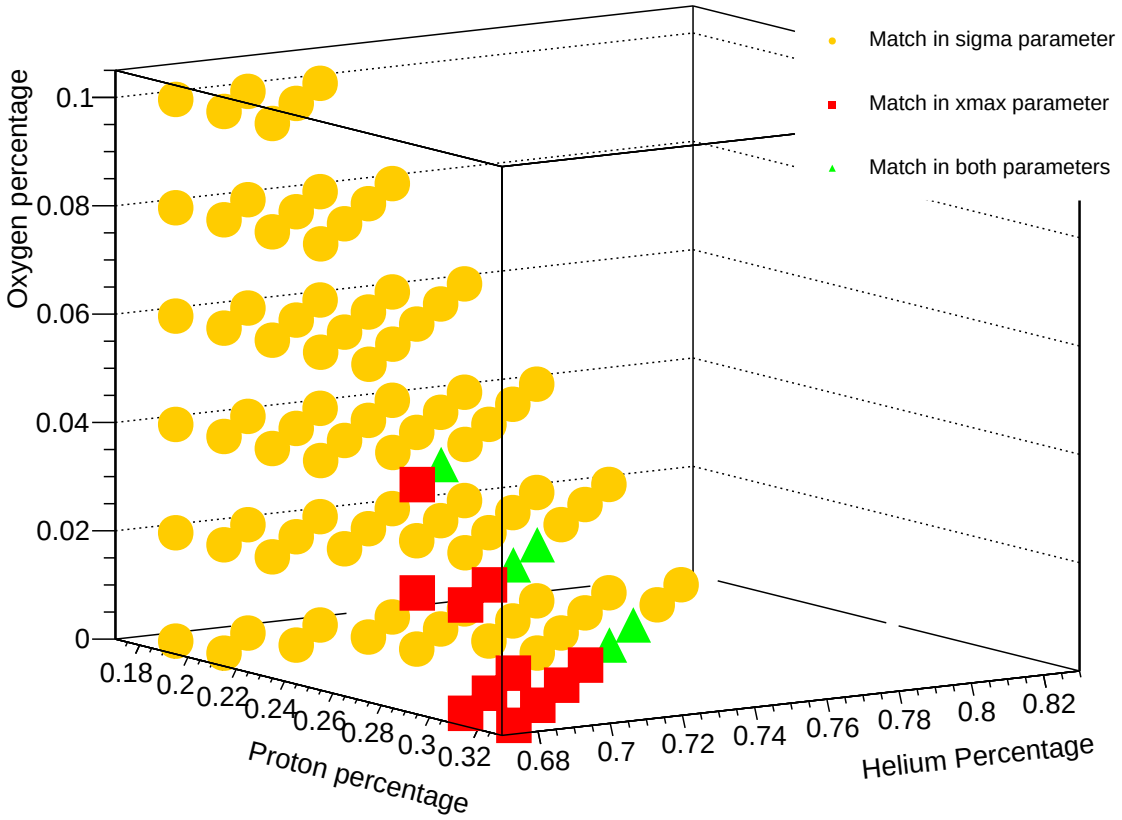

Figure 6.11.: *Visual representation of all possible combinations of simulated protons, helium, oxygen and iron which correspond to the Auger data(2017) [33] in either $\langle X_{max} \rangle$, $\sigma(X_{max})$ or both, with a focus on the area in which mixtures are accepted in both parameters. The value of κ used for the simulations is -3×10^{-20}. The Auger data compared to is the energy bin $E_{Hadron} = 1 \times 10^{19.34}\,\mathrm{eV}$.*

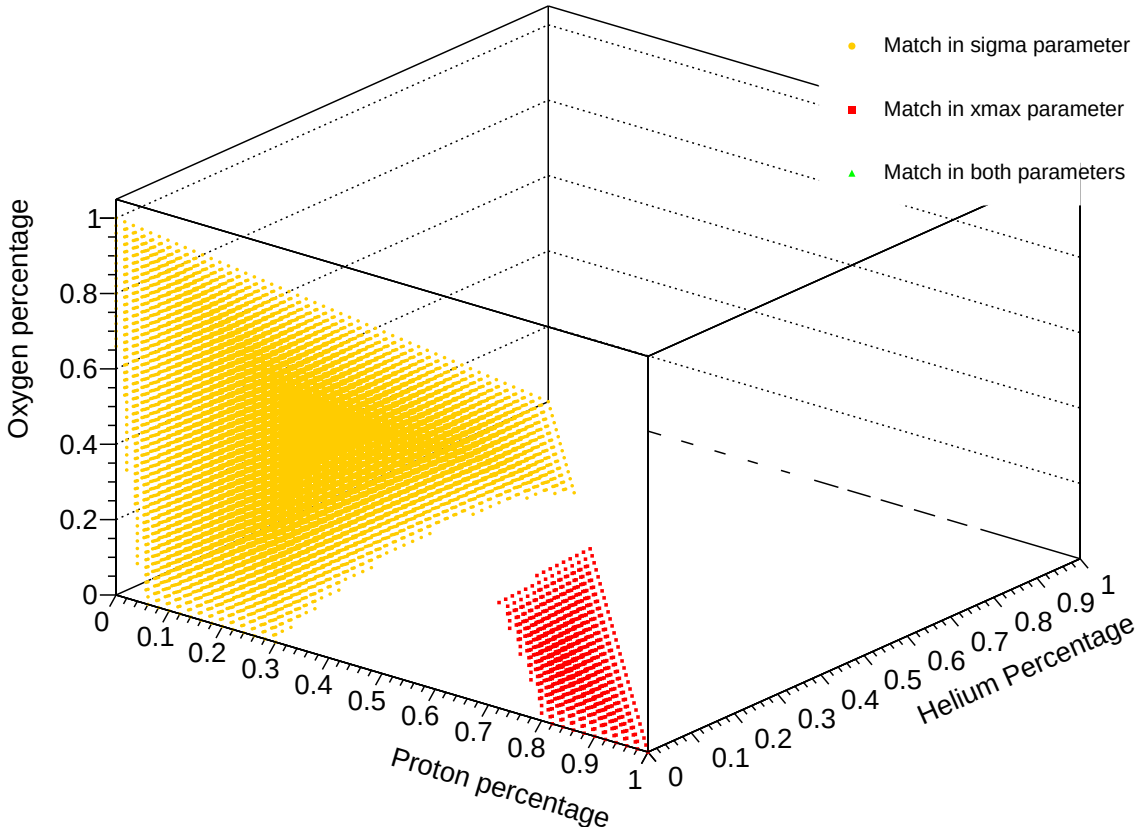

Figure 6.12.: *Visual representation of all possible combinations of simulated protons, helium, oxygen and iron which correspond to the Auger data in either* $\langle X_{max} \rangle$*,* $\sigma(X_{max})$ *or both. The value of* κ *used for the simulations is* -5×10^{-20}*. The Auger data compared to is the energy bin* $E_{Hadron} = 1 \times 10^{19.34}\,\mathrm{eV}$*.*

7. Summary and Outlook

The goal of this thesis was the improvement of the bounds on isotropic nonbirefringent LV in the photon sector using air shower simulations through the CONEX code. The method used to determine bounds closer to zero was the expansion of already existing methods by including the possibility of different primary elements of cosmic rays. The first chapters cover the theory behind the modified Maxwell theory used (Cha. 2), as well as a general introduction into cosmic rays (Cha. 3) and the Pierre Auger Observatory (Cha. 4). The changes implemented in the CONEX simulation code in order to include LV are discussed in Cha. 5. Using the modified CONEX code, air shower simulations for different primary elements and energies were done using different values of the LV parameter κ.

Different methods are explored to improve the bound $\kappa > -3 \times 10^{-19}$ determined in [1]. In Sec. 6.2 the analysis is restrained to a pure proton composition, using only the air shower parameter $\langle X_{\max} \rangle$ to determine a lower limit of $\kappa > -2 \times 10^{-19}$. This limit is determined by comparing the simulated values of $\langle X_{\max} \rangle$ to measurements of $\langle X_{\max} \rangle$ performed by the Pierre Auger Observatory, using a one sided test against a confidence level of 98 %. A similar approach is used in Sec. 6.3 with the primary cosmic elements assumed to be either protons or iron nuclei. The shower parameters $\langle X_{\max} \rangle$ and $\sigma(X_{\max})$ are used together to determine which values of κ are compatible with the Auger Data. The conclusion is that a combination of only protons and iron nuclei as primary cosmic rays is not possible for any value of κ, including the SM assumption of $\kappa = 0$.

In Sec. 6.4 the number of possible primary elements is increased to four. Now any combination of protons, helium, oxygen and iron nuclei is possible while each of those elements is representing their element group. When comparing all possible combinations of elements simulated using a certain value of κ to the Auger Data, it was found that values of $\kappa \geq -3 \times 10^{-20}$ are in accordance with the Auger Data but those samples with $\kappa \leq -5 \times 10^{-20}$ are not. This leads to the new limit of $\kappa \geq -5 \times 10^{-20}$. This limit is almost one order of magnitude smaller than the previous limit of $\kappa \geq -3 \times 10^{-19}$ and corresponds to a photon threshold energy of over 3 PeV.

Which combinations of primary elements are accepted as matching the Auger data is the next step in this analysis. Accepted combinations in both $\langle X_{\max} \rangle$ and $\sigma(X_{\max})$ form coherent subspaces in the phasespace of all possible combinations. Combinations for which both observables are accepted exist as soon as those subspaces overlap. A further analysis

of this behaviour could be used to improve the bound on κ. Other hadronic interaction models can also be taken into account to decrease systematic uncertainties, thus again improving the bound on κ.

A. Tables of Results

Here, additional tables containing all results are displayed. Tabs. A.1 and A.2 contain the results under the assumption a pure proton-iron composition. Tabs. A.3 through A.5 contain all result of the analysis with all four primary elements.

$log_{10}(E_{\mathrm{Hadron}}[\mathrm{eV}])$	$\kappa = -3 \times 10^{-19}$			$\kappa = -1 \times 10^{-19}$			$\kappa = -3 \times 10^{-20}$			$\kappa = -1 \times 10^{-20}$		
	Accepted for			Accepted for			Accepted for			Accepted for		
	Both	$\langle X_{\mathrm{max}} \rangle$	$\sigma(X_{\mathrm{max}})$	Both	$\langle X_{\mathrm{max}} \rangle$	$\sigma(X_{\mathrm{max}})$	Both	$\langle X_{\mathrm{max}} \rangle$	$\sigma(X_{\mathrm{max}})$	Both	$\langle X_{\mathrm{max}} \rangle$	$\sigma(X_{\mathrm{max}})$
17.26	29	29	36	30	30	36	28	28	38	27	27	39
17.35	22	22	29	25	25	29	27	27	32	28	28	33
17.45	24	24	33	27	27	34	13	28	22	14	28	23
17.55	22	22	31	25	25	32	27	27	35	28	28	35
17.65	7	21	18	24	24	33	7	27	15	9	28	17
17.75	16	16	27	19	19	27	23	23	31	25	25	32
17.85	13	13	26	17	17	25	21	21	29	23	23	30
17.95	9	9	23	13	13	20	18	18	26	21	21	28
18.05	5	5	22	10	10	20	15	15	25	18	18	27
18.15	1	1	23	6	6	23	12	12	26	15	15	27
18.25	0	0	14	3	3	17	9	9	21	9	12	17
18.35	0	0	22	2	2	25	8	8	27	12	12	25
18.45	0	0	26	0	0	29	6	6	30	9	9	28
18.55	0	0	29	3	3	32	8	8	33	11	11	31
18.65	0	0	32	2	2	34	8	8	35	11	11	34
18.75	0	1	16	0	7	13	0	12	13	0	16	13
18.85	0	0	11	0	5	9	0	10	10	0	14	9
18.95	0	0	16	0	6	12	0	12	14	0	16	13
19.05	0	0	29	0	4	20	1	10	27	0	14	21
19.15	0	3	10	0	8	9	0	14	10	0	18	9
19.24	1	1	36	0	5	28	11	11	43	9	15	37
19.34	0	3	11	0	6	12	0	13	13	0	16	13
19.45	0	5	20	0	8	23	0	14	24	0	18	27
19.63	0	10	7	0	14	7	0	20	7	0	24	8

Table A.1.: *Result of both the $\langle X_{max} \rangle$ and $\sigma(X_{max})$ analysis for all combinations of protons and iron. For each value of E_{Hadron} and κ the number of results of the modified simulation matching the Auger Data (2017) [33] can be seen. The simulated shower observables match the Auger Data in all energy bins for no κ value.*

$log_{10}(E_{\text{Hadron}}[\text{eV}])$	$\kappa = -1 \times 10^{-21}$			$\kappa = -1 \times 10^{-22}$		
	Accepted for			Accepted for		
	Both	$\langle X_{\text{max}} \rangle$	$\sigma(X_{\text{max}})$	Both	$\langle X_{\text{max}} \rangle$	$\sigma(X_{\text{max}})$
17.26	9	25	21	9	25	21
17.35	24	25	36	14	24	27
17.45	1	25	10	0	24	9
17.55	3	25	14	1	25	10
17.65	0	25	8	0	24	6
17.75	25	27	34	8	25	21
17.85	4	26	13	0	24	10
17.95	14	25	22	5	25	16
18.05	22	22	32	11	25	21
18.15	20	20	33	10	23	22
18.25	19	19	29	22	22	33
18.35	19	19	32	12	22	26
18.45	18	18	34	6	21	18
18.55	20	20	36	4	23	17
18.65	20	20	37	8	24	24
18.75	0	24	11	0	28	9
18.85	0	23	9	0	27	7
18.95	0	25	11	0	29	9
19.05	0	23	19	0	28	15
19.15	0	27	8	0	32	7
19.24	8	25	27	11	31	25
19.34	0	27	11	0	33	10
19.45	2	28	21	7	35	19
19.63	0	34	7	0	37	6

Table A.2.: *Result of both the $\langle X_{max} \rangle$ and $\sigma(X_{max})$ analysis for all combinations of protons and iron. For each value of E_{Hadron} and κ the number of results of the modified simulation matching the Auger Data (2017) [33] can be seen. The simulated shower observables match the Auger Data in all energy bins for no κ value.*

$log_{10}(E_{\mathrm{Hadron}}[\mathrm{eV}])$	$\kappa = -4 \times 10^{-19}$			$\kappa = -3 \times 10^{-19}$			$\kappa = -2 \times 10^{-19}$			$\kappa = -1 \times 10^{-19}$		
	Accepted for			Accepted for			Accepted for			Accepted for		
	Both	$\langle X_{\mathrm{max}} \rangle$	$\sigma(X_{\mathrm{max}})$	Both	$\langle X_{\mathrm{max}} \rangle$	$\sigma(X_{\mathrm{max}})$	Both	$\langle X_{\mathrm{max}} \rangle$	$\sigma(X_{\mathrm{max}})$	Both	$\langle X_{\mathrm{max}} \rangle$	$\sigma(X_{\mathrm{max}})$
17.26	5789	15892	5936	8396	16717	8729	7619	17618	7778	8162	18385	8325
17.35	754	8632	768	2640	9999	2799	1567	10972	1601	2243	12726	2302
17.45	3718	10170	4109	5430	11492	6090	4450	12398	4777	5764	14436	6147
17.55	2725	8341	3034	4020	9699	4532	3097	10650	3316	4273	13046	4544
17.65	3483	6982	4371	4368	8200	5470	3952	9385	4573	4787	11789	5332
17.75	1363	3309	1823	1857	4065	2522	1555	5380	1846	1719	7625	1932
17.85	1001	1895	1581	1249	2302	2004	1169	3452	1525	992	5288	1158
17.95	574	876	1173	604	905	1314	691	1745	1045	325	2899	399
18.05	207	218	1188	170	178	1117	385	561	992	218	1089	373
18.15	11	11	1642	6	6	1331	87	87	1366	224	291	1013
18.25	0	0	316	0	0	95	1	1	150	28	48	176
18.35	0	0	1687	0	0	971	0	0	1273	23	23	1773
18.45	0	0	3288	0	0	2249	0	0	2717	0	0	3796
18.55	0	0	5213	0	0	4073	0	0	4611	23	23	5965
18.65	0	0	7260	0	0	6291	0	0	6774	15	15	7999
18.75	0	0	13406	0	1	14456	0	42	13552	0	286	12712
18.85	0	0	11995	0	0	13072	0	7	12194	0	110	11150
18.95	0	0	15916	0	0	16980	0	37	16025	0	216	14849
19.05	0	0	17832	0	0	17993	0	2	17853	0	59	16754
19.15	0	11	11263	0	34	11025	0	127	10913	0	445	10896
19.24	0	0	20359	2	2	20496	12	12	20288	60	121	19919
19.34	0	0	14545	0	34	12830	0	49	13818	0	248	13834
19.45	2	2	22799	0	133	20428	13	118	21904	63	416	21389
19.63	0	305	2653	0	900	2542	0	1072	2758	0	2208	3024

Table A.3.: *Result of both the $\langle X_{max} \rangle$ and $\sigma(X_{max})$ analysis for all combinations of all four elements. For each value of E_{Hadron} and κ the number of results of the modified simulation matching the Auger Data (2017) [33] can be seen. The simulated shower observables match the Auger Data in all energy bins only for $\kappa \geq -3 \times 10^{-20}$.*

$log_{10}(E_{\text{Hadron}}[\text{eV}])$	$\kappa = -5 \times 10^{-20}$			$\kappa = -3 \times 10^{-20}$			$\kappa = -1 \times 10^{-20}$			$\kappa = -1 \times 10^{-21}$		
	Accepted for			Accepted for			Accepted for			Accepted for		
	Both	$\langle X_{\text{max}} \rangle$	$\sigma(X_{\text{max}})$	Both	$\langle X_{\text{max}} \rangle$	$\sigma(X_{\text{max}})$	Both	$\langle X_{\text{max}} \rangle$	$\sigma(X_{\text{max}})$	Both	$\langle X_{\text{max}} \rangle$	$\sigma(X_{\text{max}})$
17.26	8459	18782	8622	9872	18950	10231	11035	19355	11502	11877	19101	13142
17.35	2182	13409	2228	3666	14251	3822	4382	15278	45275	6877	16181	7387
17.45	5802	15098	6116	7496	15948	8021	8500	17014	8942	8937	17550	9842
17.55	4371	13919	4580	6044	15007	6423	6687	16295	6985	8444	17198	9185
17.65	5274	13030	5738	6350	14246	6959	7190	15765	7697	7686	17062	8478
17.75	2299	9292	2516	3098	10748	3400	3498	12739	3748	6276	14913	6811
17.85	1735	7287	1963	2156	8738	2409	2551	11075	2778	4690	13803	5188
17.95	1064	5012	1259	1151	6290	1315	1469	8939	1642	3652	12259	4075
18.05	801	2672	1154	891	3631	1182	1045	6243	1286	3041	10191	3610
18.15	727	1159	1667	961	1728	1911	1048	3753	1594	3115	8146	4144
18.25	111	433	272	282	733	599	65	2065	107	1285	6490	1676
18.35	269	286	1722	491	530	2441	602	1632	1187	2622	6390	3800
18.45	99	99	3384	209	209	4409	717	884	2590	3314	5428	5740
18.55	246	246	5413	493	493	6303	1360	1509	4642	4943	7312	7808
18.65	236	236	7592	439	439	7981	1385	1402	7049	5721	7338	9771
18.75	83	973	12976	398	1610	13330	1990	3632	13501	7422	11286	14012
18.85	0	586	11379	14	1012	12056	364	2596	11747	4635	10162	11967
18.95	1	885	15055	175	1436	16229	866	3428	15290	7030	11782	15523
19.05	140	456	17195	777	816	17683	1583	2235	16876	9371	10215	18153
19.15	0	1355	10965	1	2286	11477	236	4803	11389	3385	14178	10167
19.24	622	622	20027	1219	1219	20133	2895	2901	19730	11823	11938	20565
19.34	0	922	14393	5	1808	14208	294	3847	14799	4688	13657	13121
19.45	863	1263	22162	1754	2486	21867	4281	4869	22028	13450	15253	21094
19.63	0	4148	3225	0	6459	2901	0	10369	3554	961	19827	2886

Table A.4.: *Result of both the $\langle X_{max} \rangle$ and $\sigma(X_{max})$ analysis for all combinations of all four elements. For each value of E_{Hadron} and κ the number of results of the modified simulation matching the Auger Data (2017) [33] can be seen. The simulated shower observables match the Auger Data in all energy bins only for $\kappa \geq -3 \times 10^{-20}$.*

$log_{10}(E_{\mathrm{Hadron}}[\mathrm{eV}])$	$\kappa = -1 \times 10^{-22}$		
	Accepted for		
	Both	$\langle X_{\mathrm{max}} \rangle$	$\sigma(X_{\mathrm{max}})$
17.26	11966	19052	13228
17.35	7305	16095	7910
17.45	8671	17385	9649
17.55	8510	17134	9435
17.65	7520	17123	8478
17.75	7661	15468	8438
17.85	5667	14725	6385
17.95	5152	13635	5773
18.05	4765	12045	5590
18.15	4978	10398	6416
18.25	2833	9058	3619
18.35	4746	9197	6517
18.45	5513	8493	8673
18.55	7364	10713	10651
18.65	8858	11283	12828
18.75	8905	15309	13499
18.85	6406	14938	10982
18.95	9461	16795	14155
19.05	13778	16004	18558
19.15	5144	19064	8418
19.24	17131	17784	21096
19.34	8317	19189	12209
19.45	18587	20368	21318
19.63	1805	22560	2475

Table A.5.: *Result of both the $\langle X_{max} \rangle$ and $\sigma(X_{max})$ analysis for all combinations of all four elements. For each value of E_{Hadron} and κ the number of results of the modified simulation matching the Auger Data (2017) [33] can be seen. The simulated shower observables match the Auger Data in all energy bins only for $\kappa \geq -3 \times 10^{-20}$.*

B. Additional Figures

Here, additional figures are displayed to show the change in possible combinations of the four elements for a fixed energy bin with changing value of κ. Figs. B.1 through B.6 show the results for κ values progressively closer to 0.

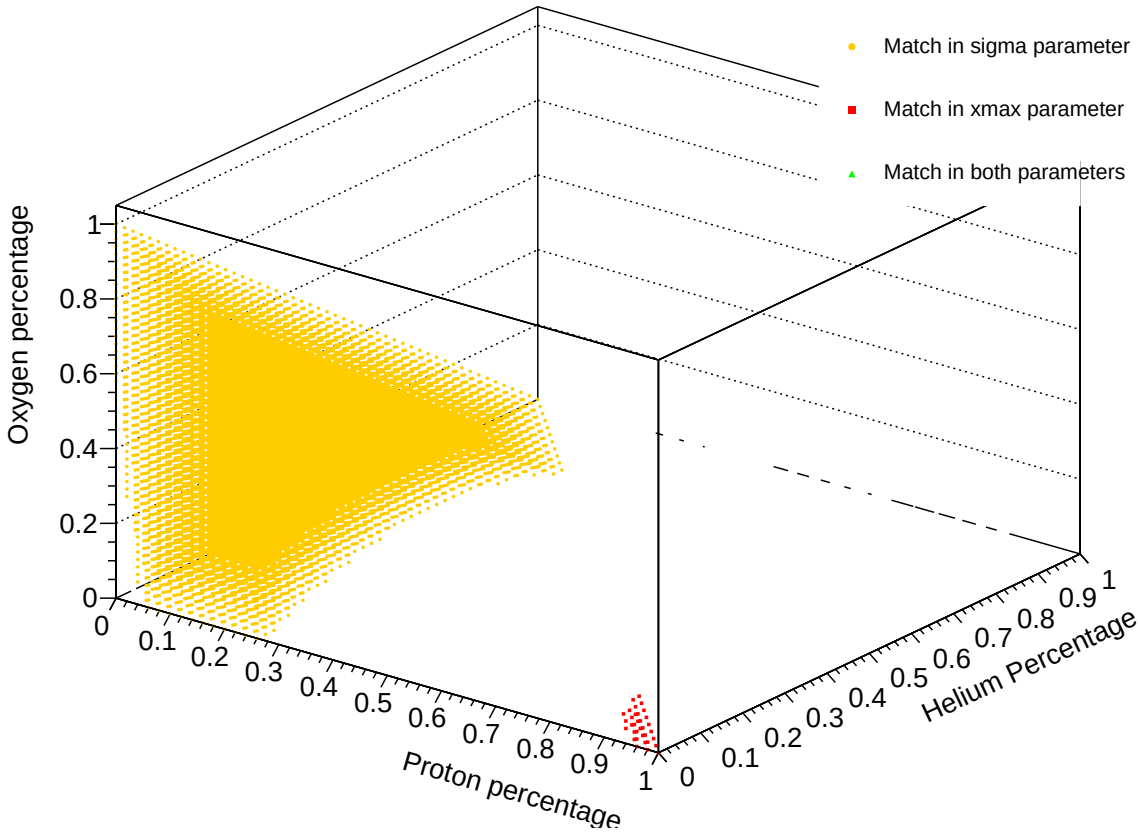

Figure B.1.: *Visual representation of all possible combinations of simulated protons, helium, oxygen and iron which correspond to the Auger data in either* $\langle X_{max} \rangle$, $\sigma(X_{max})$ *or both. The value of* κ *used for the simulations is* -3×10^{-19}. *The Auger data compared to is the energy bin* $E_{Hadron} = 1 \times 10^{19.34}\,\mathrm{eV}$.

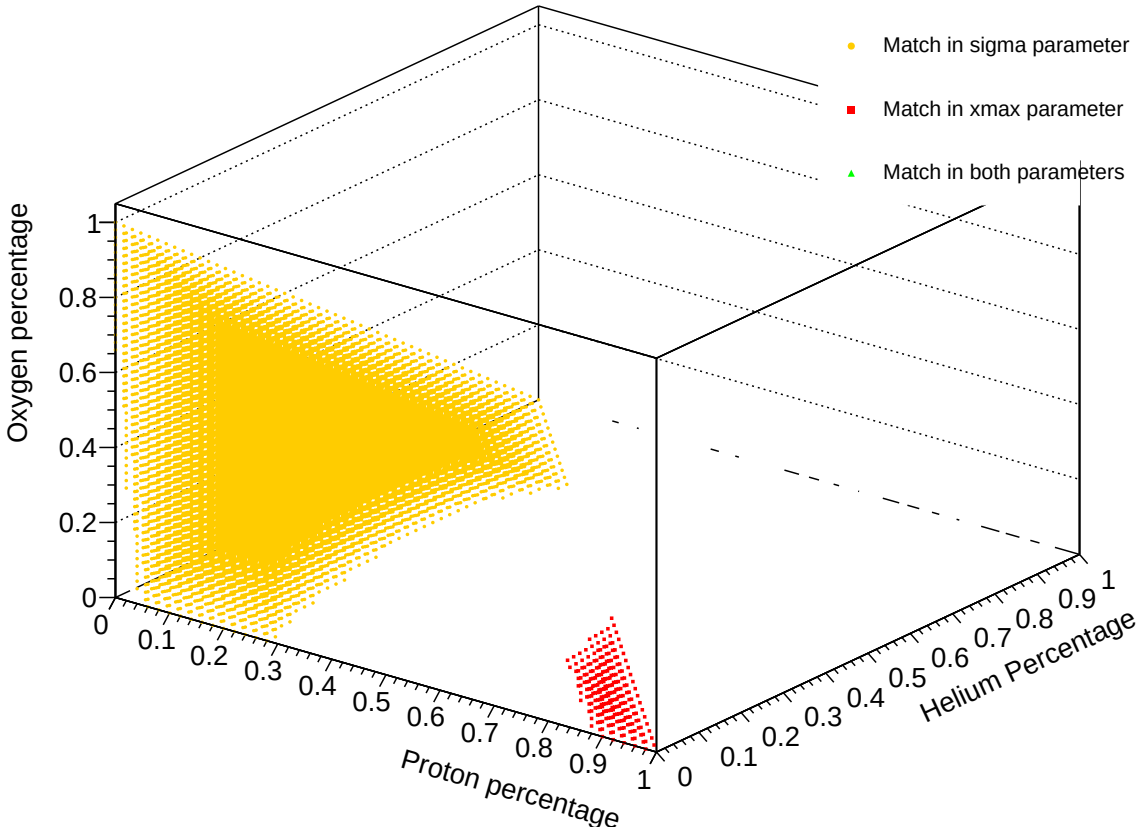

Figure B.2.: *Visual representation of all possible combinations of simulated protons, helium, oxygen and iron which correspond to the Auger data in either* $\langle X_{max} \rangle$, $\sigma(X_{max})$ *or both. The value of* κ *used for the simulations is* -1×10^{-19}. *The Auger data compared to is the energy bin* $E_{Hadron} = 1 \times 10^{19.34}\,\mathrm{eV}$.

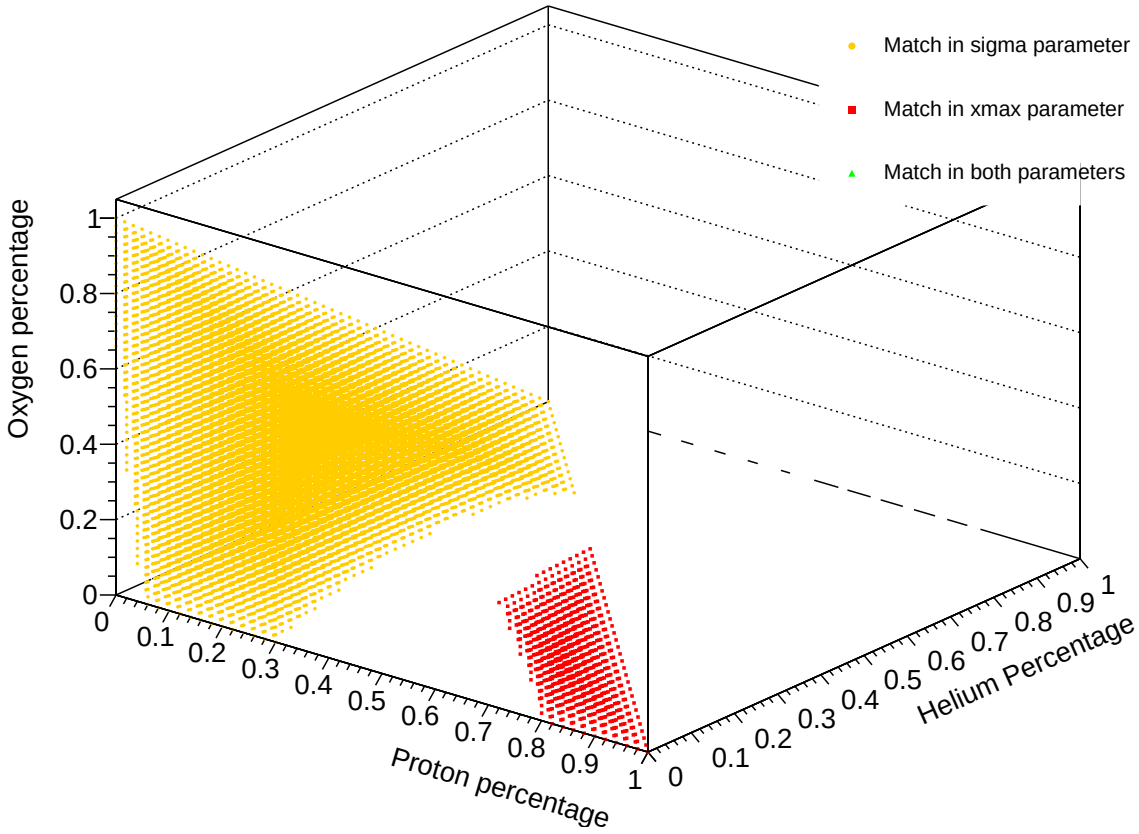

Figure B.3.: *Visual representation of all possible combinations of simulated protons, helium, oxygen and iron which correspond to the Auger data in either* $\langle X_{max} \rangle$, $\sigma(X_{max})$ *or both. The value of* κ *used for the simulations is* -5×10^{-20}. *The Auger data compared to is the energy bin* $E_{Hadron} = 1 \times 10^{19.34}\,\mathrm{eV}$.

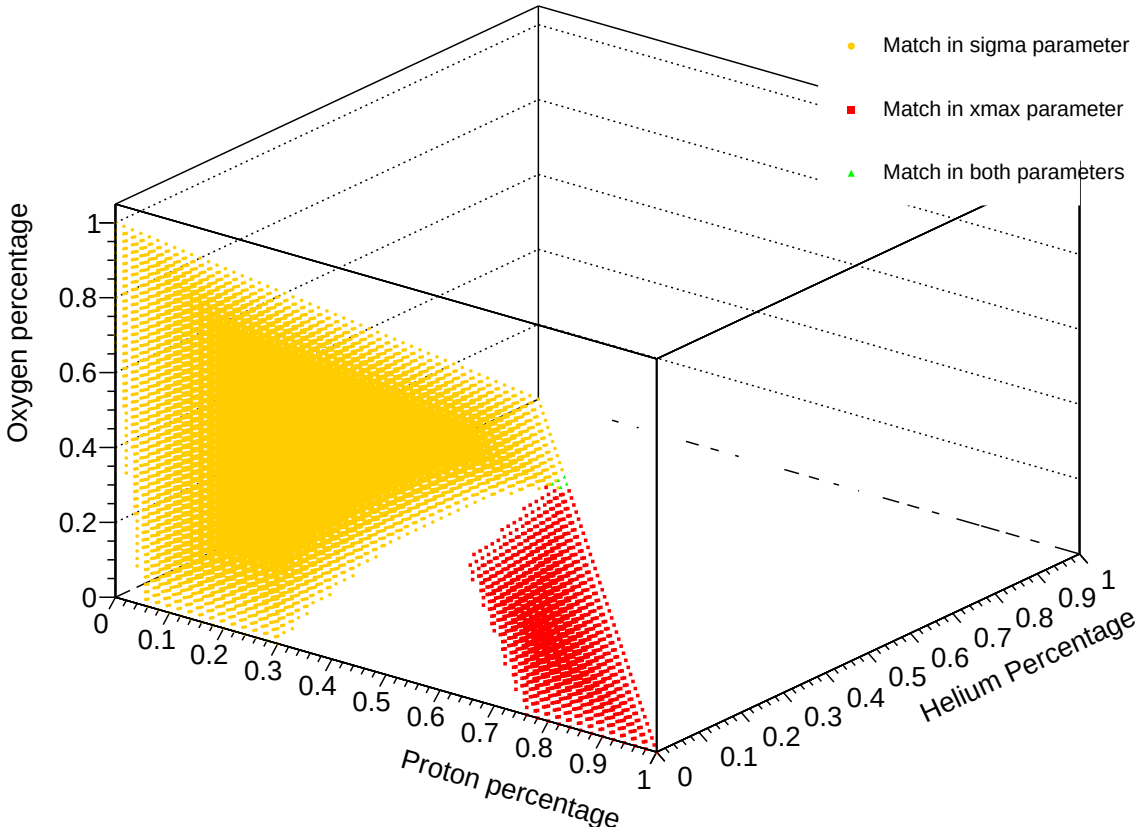

Figure B.4.: *Visual representation of all possible combinations of simulated protons, helium, oxygen and iron which correspond to the Auger data in either* $\langle X_{max} \rangle$, $\sigma(X_{max})$ *or both. The value of* κ *used for the simulations is* -3×10^{-20}. *The Auger data compared to is the energy bin* $E_{Hadron} = 1 \times 10^{19.34}\,\mathrm{eV}$.

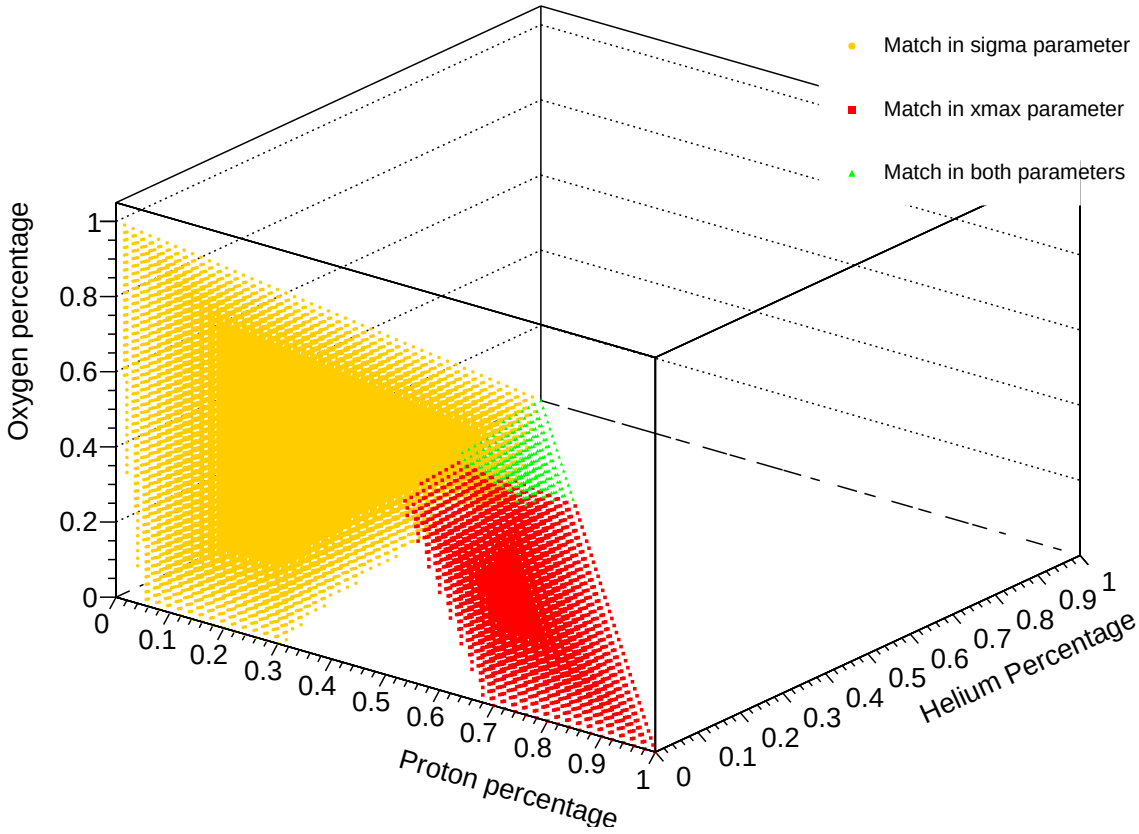

Figure B.5.: *Visual representation of all possible combinations of simulated protons, helium, oxygen and iron which correspond to the Auger data in either* $\langle X_{max} \rangle$, $\sigma(X_{max})$ *or both. The value of* κ *used for the simulations is* -1×10^{-20}. *The Auger data compared to is the energy bin* $E_{Hadron} = 1 \times 10^{19.34}\,\mathrm{eV}$.

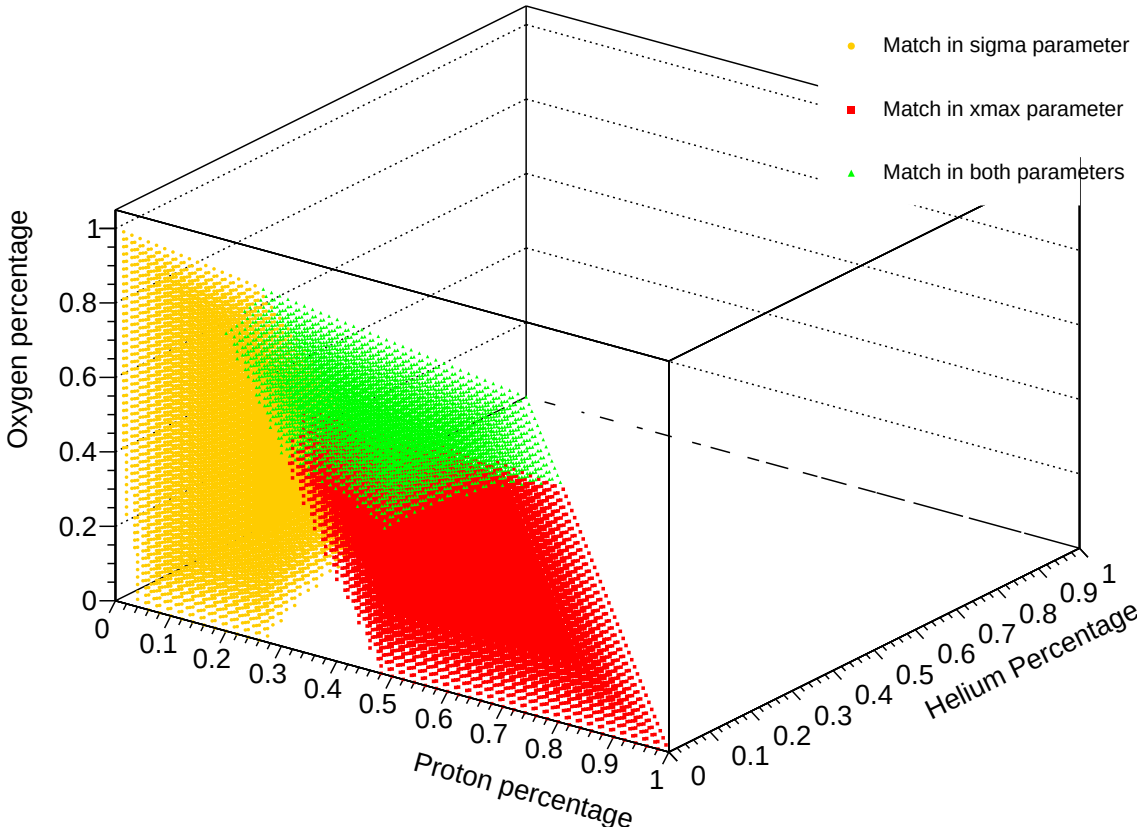

Figure B.6.: *Visual representation of all possible combinations of simulated protons, helium, oxygen and iron which correspond to the Auger data in either* $\langle X_{max} \rangle$, $\sigma(X_{max})$ *or both. The value of* κ *used for the simulations is* -1×10^{-21}. *The Auger data compared to is the energy bin* $E_{Hadron} = 1 \times 10^{19.34}\,\mathrm{eV}$.

C. List of Acronyms

AGN	Active Galactic Nucleus
CDAS	Central Data Acquisition System
CI	Confidence Interval
CL	Confidence Level
FADC	Flash Analog-to-Digital Converter
FD	Fluorescence Detector
GCR	Galactic Cosmic Ray
GPS	Global Positioning System
LV	Lorentz Violation
MC	Monte Carlo
PMT	Photo Multiplier Tube
QED	Quantum Electrodynamics
SD	Surface Detector
SM	Standard Model of Particle Physics
UHECR	Ultra-High-Energy Cosmic Ray
VEM	Vertical Equivalent Muons

D. Bibliography

[1] F. R. Klinkhamer, M. Niechciol, and M. Risse, Improved bound on isotropic Lorentz violation in the photon sector from extensive air showers, *Phys. Rev. D*, 96:116011, Dec 2017.

[2] F. R. Klinkhamer and M. Schreck, New two-sided bound on the isotropic Lorentz-violating parameter of modified Maxwell theory, *Phys. Rev. D*, 78:085026, Oct 2008.

[3] J. S. Diaz, F. R. Klinkhamer, and M. Risse, Changes in extensive air showers from isotropic Lorentz violation in the photon sector, *Phys. Rev. D*, 94:085025, 2016.

[4] A. Aab, P. Abreu, M. Aglietta, et al., Depth of maximum of air-shower profiles at the Pierre Auger Observatory. i. measurements at energies above $10^{17.8}$ eV, *Phys. Rev. D*, 90:122005, Dec 2014.

[5] T. Bergmann, R. Engel, D. Heck, et al., One-dimensional hybrid approach to extensive air shower simulation, *Astroparticle Physics*, 26(6):420 – 432, 2007.

[6] T. Pierog, M. Alekseeva, T. Bergmann, et al., First results of fast one-dimensional hybrid simulation of EAS using CONEX, *Nuclear Physics B - Proceedings Supplements*, 151(1):159 – 162, 2006.

[7] S. Chadha and H. Nielsen, Lorentz invariance as a low energy phenomenon, *Nuclear Physics B*, 217(1):125 – 144, 1983.

[8] V. A. Kostelecký and M. Mewes, Signals for Lorentz violation in electrodynamics, *Phys. Rev. D*, 66:056005, Sep 2002.

[9] F. Klinkhamer and M. Schreck, Consistency of isotropic modified Maxwell theory: Microcausality and unitarity, *Nuclear Physics B*, 848(1):90 – 107, 2011.

[10] F. R. Klinkhamer, Lorentz-violating neutral-pion decays in isotropic modified Maxwell theory, *Modern Physics Letters A*, 33, 2016.

[11] J. S. Díaz and F. R. Klinkhamer, Parton-model calculation of a nonstandard decay process in isotropic modified Maxwell theory, *Phys. Rev. D*, 92:025007, Jul 2015.

[12] M. Niechciol, Diffuse and targeted searches for ultra-high-energy photons using the hybrid detector of the Pierre Auger Observatory, *PoS*, ICRC2017:517, 2018.

[13] J. S. George, K. A. Lave, M. E. Wiedenbeck, et al., Elemental composition and energy spectra of galactic cosmic rays during solar cycle 23, *The Astrophysical Journal*, 698:1666, 06 2009.

[14] J. Bluemer, R. Engel, and J. R. Hoerandel, Cosmic rays from the knee to the highest energies, *Progress in Particle and Nuclear Physics*, 2009.

[15] M. Niechciol, private communication, 2019.

[16] K. Collaboration and T. Antoni, KASCADE measurements of energy spectra for elemental groups of cosmic rays: Results and open problems, *Astroparticle Physics*, 24:1–25, 2005.

[17] D. Kazanas and A. Nicolaidis, Cosmic ray 'knee': A Herald of new physics?, In *27th International Cosmic Ray Conference (ICRC 2001) Hamburg, Germany, August 7-15, 2001*, pages 1760–1763, 2001.

[18] F. W. Stecker and M. H. Salamon, Photodisintegration of ultrahigh energy cosmic rays: A new determination, *The Astrophysical Journal*, 512:521–526, 1998.

[19] P. Travnicek, *Detection of high-energy muons in cosmic ray showers*, PhD thesis, Prague, Inst. Phys., 2004.

[20] C. Grupen, *Astroparticle Physics*, Springer, 2005.

[21] P. K. F. Grieder, *Extensive Air Showers*, Springer, 2010.

[22] D. Veberic, Maps of the Pierre Auger Observatory, `https://web.ikp.kit.edu/darko/auger/auger-array/`, 2013.

[23] I. Allekotte, A. F. Barbosa, P. Bauleo, et al., The surface detector system of the Pierre Auger Observatory, *Nuclear Instruments and Methods in Physics*, 2007.

[24] Pierre Auger Observatory, `https://www.flickr.com/photos/134252569@N07/20048280345/in/album-72157656390939652/`, 2015.

[25] P. A. Cherenkov, Visible emission of clean liquids by action of γ radiation, *Doklady Akademii Nauk SSSR*, 2:451, 1934.

[26] J. Abraham, P. Abreu, M. Aglietta, et al., Trigger and aperture of the surface detector array of the Pierre Auger Observatory, *Nuclear Instruments and Methods in Physics*, 2011.

[27] J. Abraham, P. Abreu, M. Aglietta, et al., The fluorescence detector of the Pierre Auger Observatory, *Nuclear Instruments and Methods in Physics*, 24:1–25, 2009.

[28] T. Pierog, Air shower simulation with a new generation of post-LHC hadronic interaction models in CORSIKA, *PoS*, ICRC2017:1100, 2018.

[29] S. Ostapchenko, Monte Carlo treatment of hadronic interactions in enhanced pomeron scheme: QGSJET-II model, *Phys. Rev. D*, 83:014018, Jan 2011.

[30] F. Riehn, H. P. Dembinski, R. Engel, et al., The hadronic interaction model SIBYLL 2.3c and Feynman scaling, 2017.

[31] M. D. Domenico, M. Settimo, S. Riggi, and E. Bertin, Reinterpreting the development of extensive air showers initiated by nuclei and photons, *Journal of Cosmology and Astroparticle Physics*, 2013.

[32] E.-J. Ahn, R. Engel, T. K. Gaisser, P. Lipari, and T. Stanev, Cosmic ray interaction event generator SIBYLL 2.1, *Phys. Rev. D*, 80:094003, Nov 2009.

[33] J. Bellido, Depth of maximum of air-shower profiles at the Pierre Auger Observatory: Measurements above $10^{17.2}$ eV and composition implications, *PoS*, ICRC2017:506, 2018.

Danksagung

Am Ende dieser Arbeit möchte ich den Personen danken, die mich bei der Erstellung dieser Arbeit unterstützt haben.

Zunächst möchte ich mich bei Prof. Dr. Markus Risse bedanken, durch den es mir möglich war, in der Arbeitsgruppe Experimentelle Teilchenphysik diese Masterarbeit zu schreiben.

Mein besonderer Dank gilt meinem Büronachbarn Dr. Marcus Niechciol für seine Anleitung und die vielen Gespräche, die bei der Erstellung dieser Arbeit geholfen haben.

Der gesamten Arbeitsgruppe Experimentelle Teilchenphysik möchte ich für das angenehme Arbeitsklima danken, sowie dafür dass sie mir bei Fragen immer hilfreich zur Seite standen.

Ich danke ebenso meiner Familie und Freunden, die mich während der gesamten Arbeit durch Korrekturlesen und ermunternde Worte unterstützt haben.

Erklärung

Hiermit erkläre ich, dass ich die vorliegende Masterarbeit selbstständig verfasst und keine anderen als die angegebenen Quellen und Hilfsmittel benutzt sowie Zitate und Ergebnisse Anderer kenntlich gemacht habe.

Ort, Datum	Unterschrift